



Cite this: DOI: 10.1039/d5mh01784j

## Boosting mechanical-to-ionic transduction for self-powered piezionic sensing

Juan A. Guerrero, <sup>a</sup> Cédric Plesse, <sup>b</sup> Vladislav Y. Shevtsov, <sup>cd</sup>  
Alexander S. Shaplov, <sup>c</sup> Jean-Marie Raquez <sup>a</sup> and Jérémie Odent <sup>\*,a</sup>

In the realm of sensing, piezionic systems have emerged as innovative tools for perceiving tactile sensations through mechanical-to-ionic transduction, mimicking biological signal production and transmission. To date, the biomimetic transduction mechanism and strategies for engineering the transduction efficiency remain not fully understood and underutilized. This review provides the fundamentals of mechanical-to-ionic transduction for efficient self-powered sensing, identifying the most crucial structural and operating parameters governing the generation of a transient signal output with respect to the migration and redistribution of ions upon mechanical stimulation. It also examines the recent strategies for efficiently converting mechanical keystrokes into electrical signals through performance-driven structural design, thereby maximizing piezionic voltage generation. This involves engineering ion transport and fluid flow through porosity, microphase separation, conductive pathways and structural gradients. With respect to piezionic effect-based applications, this review highlights the promising potential of polymeric, ionic materials in soft wearable electronics, ionic skins, tissue engineering, biointerfaces and energy harvesting.

Received 18th September 2025,  
Accepted 14th November 2025

DOI: 10.1039/d5mh01784j

rsc.li/materials-horizons

### Wider impact

Piezionic materials operate through mechanical-to-ionic transduction, generating transient voltages as ions of different mobilities separate under mechanical stimulation. Although the piezionic effect is relatively new and its working principle is not yet fully understood, this review provides both material structural design guidelines for enhancing device performance and fundamental insights into the underlying transduction mechanisms. In addition, it outlines conceptual frameworks for translating the piezionic effect into practical devices, emphasizing the role of operating parameters in voltage generation and strategies for engineering fluid-driven ion transport to further boost piezionic responses.

## From cellular mechanotransduction to biomimetic electromechanical transducers

Mechanotransduction is the process by which cells sense a mechanical force and convert it into a biochemical response.<sup>1</sup> As a cornerstone of the somatosensory system, this process

supports critical physiological functions at various levels from whole-body systems to cellular and molecular processes including hearing, touch perception, and muscle contraction.<sup>1,2</sup> Maksimovic *et al.*<sup>3</sup> identified key proteins in skin mechanoreceptors that display touch-activated ionic currents, facilitating high spatio-temporal acuity for tactile perception. Under mechanical stimulation, the mechanosensitive ion-channel-based receptors transition between open and closed states. This creates an ion influx and generates an action potential which is relayed to the brain by the somatosensory system (Fig. 1).<sup>3–5</sup> Low-threshold mechanoreceptors are adapted to detect a particular stimulus and have a working range of frequency.<sup>6–8</sup> Merkel cell receptors optimally detect pressures below 2 Hz, Meissner corpuscles respond best to skin movement and dynamic motion at 2–40 Hz, and Pacinian corpuscles are tuned to vibrations within a 40–200 Hz range.<sup>8</sup> Inspired by these natural mechanisms, soft electromechanical transducers have been designed for detecting small changes in force, displacement, or vibration, converting the resulting mechanical stimuli

<sup>a</sup> Laboratory of Polymeric and Composite Materials (LPCM), Center of Innovation and Research in Materials and Polymers (CIRMAP), University of Mons (UMONS), Place du Parc 20, Mons, 7000, Belgium. E-mail: jeremy.odent@umons.ac.be

<sup>b</sup> Laboratoire de physicochimie des polymères et des interfaces (LPPI)-LPPI, CY Cergy Paris Université, 5 mail Gay Lussac, Cergy-Pontoise Cedex F-95000, France

<sup>c</sup> Functional Polymeric and Particulate Materials Unit, Luxembourg Institute of Science and Technology (LIST), 5 avenue des Hauts-Fourneaux, L-4362 Esch-sur-Alzette, Luxembourg

<sup>d</sup> Department of Physics and Materials Science, University of Luxembourg, 2 Avenue de l'Université, L-4365 Esch-sur-Alzette, Luxembourg



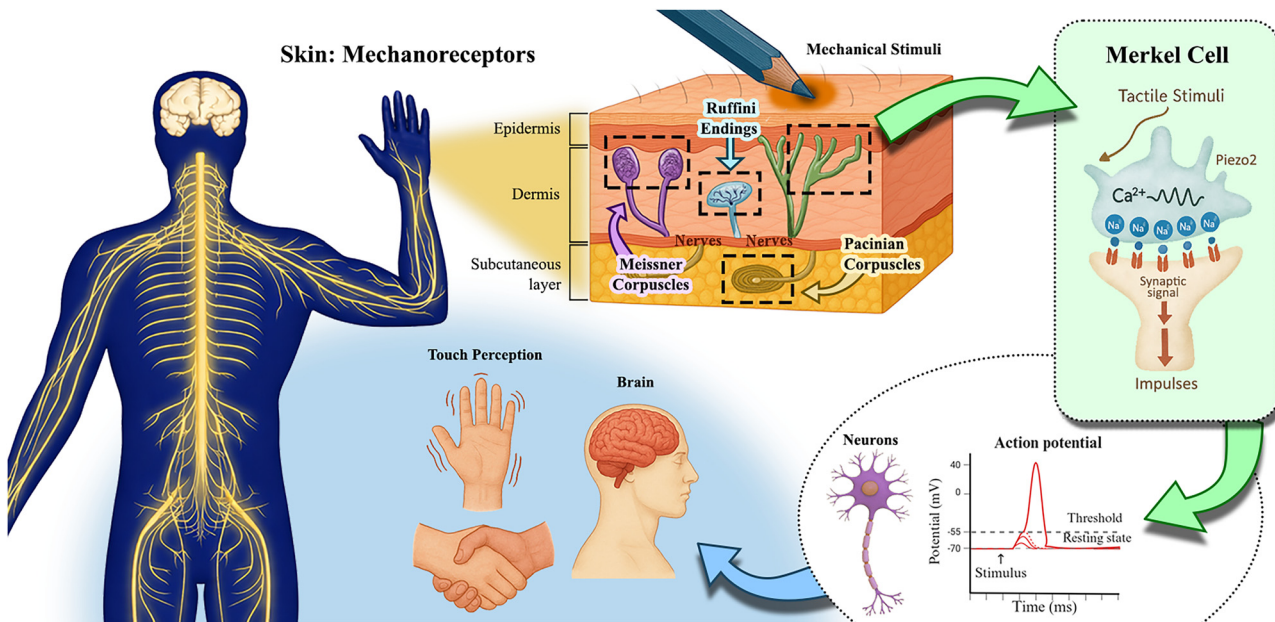


Fig. 1 Mechanisms underlying the tactile perception and the different low-threshold mechanoreceptors on skin. Human skin mechanoreceptors transduce tactile stimuli into action potentials, which are transmitted *via* the afferent nervous system to synaptic junctions. At the synapses, action potentials relay the information to the brain, giving rise to a complex multilevel feature of tactile perception.

Table 1 Conceptual distinction between piezoresistive, piezocapacitive, piezoelectric and piezionic electromechanical transducers

	Piezoresistive	Piezocapacitive	Piezoelectric	Piezionic
Transduction mechanism	Change in the percolation or conductive pathways	Alterations in plate distance or electrical permittivity	Change in polarization	Ion redistribution
Signal output	Change in resistance ( $\Delta R$ ) Current change ( $\Delta I$ )	Change in capacitance ( $\Delta C$ )	Voltage generation (V) Current change ( $\Delta I$ )	Ionic potential change ( $\Delta V$ ) Current change ( $\Delta I$ )
Signal output range	10–10 000 $\Omega$	0.001–1 nF	0.01–10 V	1–500 mV
Detection pressure range	1 Pa–1 MPa	1 Pa–1 MPa	100 Pa–10 MPa	1 Pa–100 kPa
Sensitivity	$1\text{--}1000\text{ kPa}^{-1}$	$1\text{--}100\text{ kPa}^{-1}$	$0.1\text{--}100\text{ kPa}^{-1}$	$0.001\text{--}100\text{ kPa}^{-1}$
Response time	ms–s	ms–s	ms	ms–s
Recovery time	ms	ms	ms	0.1 s–10 s
Advantages	Good stability	Good temperature independence Low power consumption	Self-powered Mechanical and chemical stability High output voltage	Self-powered Good linearity Mechanically soft and deformable
Disadvantages	Temperature sensitive High hysteresis Poor linearity Long relaxation time External power supply required	Prone to hysteresis and to interferences External power supply required	Only detect dynamic or transient loads Poling required Mechanically rigid	Moisture and temperature sensitive Low output voltage

into electrical signals.<sup>9</sup> While being increasingly valued for applications ranging from soft robotics to health monitoring, their most common transduction mechanisms include, until recently,

piezoresistive, piezocapacitive, and piezoelectric mechanisms (Table 1).<sup>10–13</sup> Despite their sensitivity to temperature, high hysteresis, poor linearity and long relaxation times, piezoresistive



transducers are capable of functioning over a wide range of detection-measuring pressures (*ca.* 1 Pa–1 MPa) due to changes in resistance as a result of local mechanical deformations.<sup>14–19</sup> Piezocapacitive transducers, are still prone to hysteresis and to interferences (such as parasitic charges or electromagnetic noise) and offer relatively high sensitivity to small pressures (*ca.* 1 Pa–1 MPa), good temperature independence, and low power consumption. These features rely on the formation of an electrical double layer (EDL) at the dielectric–electrode interface, which can detect changes in capacitance through alterations in plate distance or electrical permittivity.<sup>20–27</sup> Distinguished by their high sensitivity, fast response time, mechanical flexibility, and chemical stability, piezoelectric transducers employ the ferroelectric properties of some (semi-)crystalline and glassy materials to generate electrical charges caused by stress-induced dipole rearrangement under dynamic or transient loads.<sup>28–35</sup> However, to achieve optimal piezoelectric performance, these materials require a poling step to align the dipole within the materials, and the range of pressure detected is generally higher (*ca.* 100 Pa to 10 MPa).

Inspired by biological systems, ionotronic devices, which couple electron and ion movement, have led to the development of mechanical-to-ionic transducers, such as piezoinronics. These transducers operate *via* the flow of ions in a fluid or solid electrolyte.<sup>9,10,36</sup> The piezoinic effect relies on the newly discovered electromechanical conversion phenomenon that occurs when a non-uniform mechanical deformation is applied to ion-embedded materials. This generates a transient voltage based on the separation of ions (cations and anions of different mobilities in the fluid transport).<sup>37–39</sup> Often mistaken for piezocapacitive transducers due to the similarity of materials employed, piezoinic transducers afford a highly sensitive mechanical detection (*ca.* 1 Pa to 100 kPa) with a reliable linear response when converting mechanical loads into a proportional self-powered voltage output.<sup>37–46</sup> A fundamental distinction lies in the power dependence, as piezoresistive and piezocapacitive transducers require an external power supply to operate, whereas piezoelectric and piezoinic transducers are self-powered and generate an electrical signal autonomously. Additionally, piezoelectric transducers are rather rigid, crystalline materials that generate voltage (*ca.* 0.01–10 V) through an atomic dipole displacement. In contrast, piezoinic transducers rely on mechanically induced ion migration within soft, deformable, ionically conductive materials for generating a transient voltage (*ca.* 1–500 mV).<sup>37–46</sup> Up to now, piezoinic transducers exhibit a response time in the range of milliseconds to seconds, but a slow recovery time in the range of tenths of a second to tens of seconds when compared to other types of electromechanical transducers. Overall, the electro-mechanical performance of soft electromechanical transducers is dictated by major parameters, such as the sensitivity, detection limit, operating pressure range, response time, self-powering and linearity. These attributes enable soft electromechanical transducers to be easily integrated and to continuously monitor and detect a wide range of mechanical loads with high resolution.<sup>10–13</sup> To this end, Table 1 provides a conceptual comparison of different

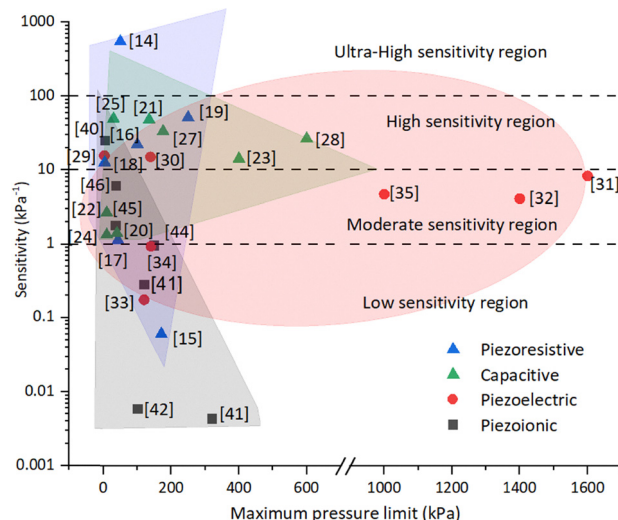


Fig. 2 Sensitivity ( $\text{kPa}^{-1}$ ) and maximum pressure limit (kPa) of common piezoresistive, capacitive, piezoelectric and piezoinic electromechanical sensors.

electromechanical transducers based on a survey of the current state-of-the-art developments in terms of their sensitivity and maximum pressure limit, as shown in Fig. 2. From an application standpoint, the detection pressure range of piezoinic transducers makes them promising candidates for wearable sensors and electronic skin technologies. Their high sensitivity to subtle forces, combined with their self-powered voltage output and good linearity, allows them to detect mechanical stimuli ranging from ultra-light touch to soft deformations, *i.e.*, well within the sensitivity range of human skin, which typically begins to perceive pressure around 10–100 Pa.

There are several reviews that previously introduced the piezoinic effect emphasizing their historical evolution, scientific description, methodology, application, and outlook.<sup>47,48</sup> Ho *et al.*<sup>47</sup> provided a holistic overview of the early conceptualization of piezoinics as a biomimetic mechanical–electrical transduction mechanism, and Chen *et al.*<sup>48</sup> highlighted the different types of piezoinic materials and methods for enhancing the piezoinic response. In contrast, this review serves as a guide for newcomers to the field as it provides insights into the fundamentals of the mechanical-to-ionic transduction, including an up-to-date description of recently used polymeric ionic materials, and the crucial structural and operating parameters governing their voltage generation. Moreover, the recent innovative strategies for engineering ion transport, fluid flow for maximizing piezoinic performance and a brief exploration of relevant applications are addressed in the review.

## Conceptual frameworks for mechanical-to-ionic transduction

Initially identified within ionic gels by De Gennes *et al.*,<sup>49</sup> the concept of mechanical-to-ionic transduction was coined as the piezoinic effect by Sarwar *et al.*<sup>37</sup> The piezoinic effect is



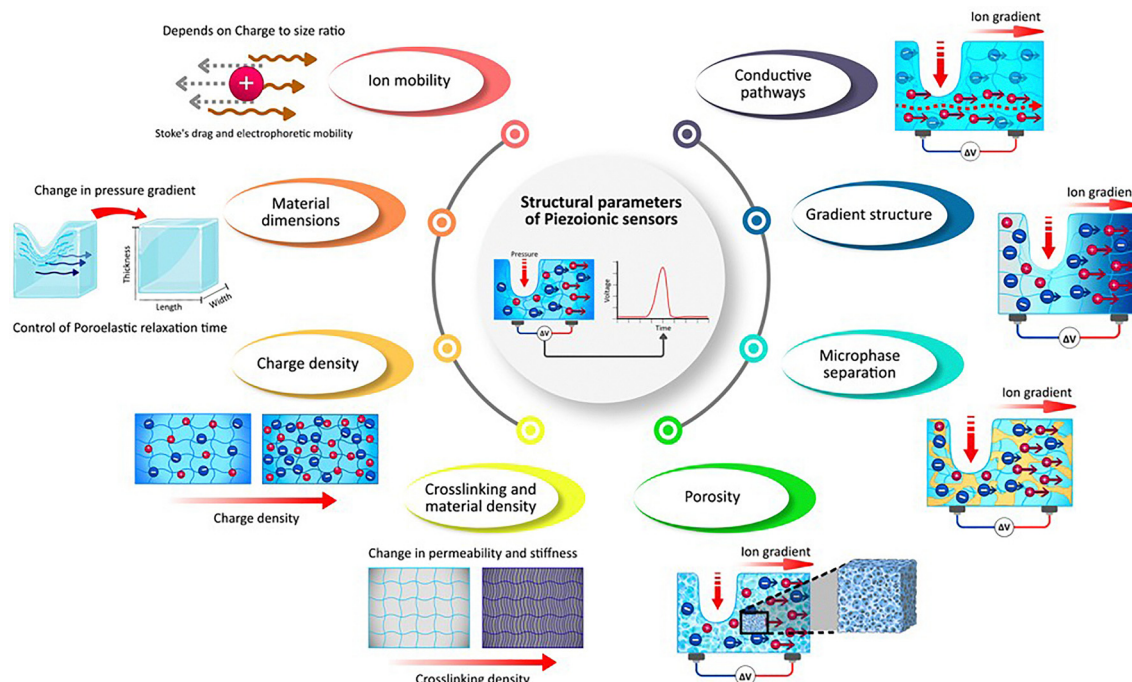


Fig. 3 Structural parameters affecting the fluid-driven ion transport, including ion mobility, material dimensions, charge density, crosslinking density, material density (left, red to yellow for material selection), porosity, microphase separation, gradient structure and conductive pathways (right, green to purple for structural design).

the transient separation between anionic and cationic species in response to an applied mechanical stress (Fig. 3).<sup>38,39</sup> Under mechanical stimulation, a fluid pressure gradient is created, which drives fluid flow within a matrix. As a result, cations and anions are carried by the fluid flow, but at different speeds due to their different mobilities and interaction with the polymer matrix. This in turn generates a transient voltage according to the leading/dominant ion (the most mobile).<sup>38,39</sup> Overall, the generated potential generally exhibits a linear relationship with the pressure gradient, as shown in eqn (1):

$$\Delta V = \alpha \Delta P \quad (1)$$

where  $\alpha$  is the piezoionic coefficient (change in output voltage per stress),  $\Delta P$  is the pressure gradient, and  $\Delta V$  is the generated potential.<sup>38</sup> Yet, the working principle of piezoinetics is not fully understood, and its theoretical foundations remain to be clarified. Nonetheless, several models have been proposed to explain the newly discovered mechanical-to-ionic transduction phenomenon. More particularly, the streaming potential<sup>44</sup> and Poisson-Nernst-Planck coupled with fluid mechanics have been developed to describe the piezoionic effect.<sup>38,39</sup> The streaming model describes the potential generated by electrolyte movement through a charged structure such as a capillary or porous medium, as defined in eqn (2):

$$\Delta V = \frac{L}{\sigma} \Delta P = \frac{N e \kappa}{\sigma \eta} \Delta P \quad (2)$$

where  $\sigma$  is the ionic conductivity,  $\Delta P$  is the pressure gradient,  $\kappa$  is the permeability,  $\eta$  is the fluid viscosity,  $N$  is the concentration of ions per cubic meter, and  $e$  is the fundamental

charge.<sup>44,49</sup> The streaming model accurately predicts the electrical potential over a broad pressure range. The streaming potential primarily arises from convective flux, where fluid movement under pressure carries ions downstream, leading to charge accumulation and electrical potential generation.<sup>44,49</sup> Although being effective for piezoionic systems built on a single mobile ion, this model is inaccurate for ion pairs (involving two mobile ions) since it only considers the transport of ions within the fluid flow due to the generation of a pressure gradient. As a result, the model suggests that the larger the fluid flow speed, the higher the piezoionic response.<sup>44,49</sup>

The Poisson-Nernst-Planck (PNP) equations are another foundation for studying ion transport in fluids, describing ionic transport under the influence of gradients and electric fields.<sup>38,39,50,51</sup> The Nernst-Planck equation considers ion transport based on the mass transport phenomena of diffusion, electromigration, and convection, whereas the Poisson equation explains the spatial charge distribution of ions, owing to an electric field; these equations are respectively shown in eqn (3) and (4), where  $J_i$  is the ion flux,  $D_i$  is the diffusion coefficient of ion  $i$ ,  $c_i$  is the concentration of such ion,  $z_i$  is the electron valence of the ion,  $k_B$  is the Boltzmann constant,  $T$  is temperature,  $e$  is the fundamental charge,  $\nu$  is the flow velocity,  $V$  is the electrical potential, and  $\epsilon$  is the permittivity of the medium:<sup>38,39,50,51</sup>

$$J_i = -D_i \nabla c_i - D_i \frac{e}{k_B T} z_i c_i \nabla V + \nu c_i \quad (3)$$

$$\nabla^2 V = \frac{\sum z_i e c_i}{\epsilon} \quad (4)$$



This model can effectively capture ion movement in biological systems, such as cells and channels.<sup>50,51</sup> Nevertheless, the PNP model has limitations, such as neglecting ion–ion interactions, steric hindrance, and finite volume effects.<sup>52,53</sup> As such, a modified PNP model considering such effects led to eqn (5) where the term  $a^3$  is the spacing between densely packed ions, which correlates to the concentration limit,  $a^3 = 1/c_{\max}$ .<sup>52,53</sup>

$$J_i = -D_i \nabla c_i - D_i \frac{e_0}{k_B T} z_i c_i \nabla V - a^3 D_i \nabla \cdot \left( \frac{c_i \nabla (c_+ + c_-)}{1 - a^3 c_+ - a^3 c_-} \right) + \nu c_i \quad (5)$$

As mechanical-to-ionic transduction critically depends on fluid flow to generate a transient voltage with respect to the transient separation of cations and anions at different speeds, it can be mechanistically analyzed by Darcy's law. The latter describes the velocity of a fluid traveling through a porous medium with respect to eqn (6), where  $\nu$  is the flow velocity,  $\kappa$  is the permeability,  $\eta$  is the viscosity, and  $\Delta P$  is the pressure gradient:<sup>38</sup>

$$\nu = -\frac{\kappa}{\eta} \Delta P \quad (6)$$

Dobashi *et al.*<sup>38</sup> combined the PNP equations (eqn (3) and (4)) with Darcy's law (eqn (6)) to better understand the mechanical-to-ionic transduction in dilute media, where ion–ion interactions are negligible, as well as for ion-pair systems (involving two mobile ions). This leads to eqn (7), where  $N$  is the number of ions,  $e$  is the fundamental charge,  $\kappa$  is the permeability,  $\eta$  is the viscosity,  $\sigma$  is the conductivity,  $D_{0+}$  and  $D_{0-}$  are the diffusion coefficients of the cation and anion without drag forces and interactions with the matrix, respectively, while  $D_+$  and  $D_-$  are the effective diffusion coefficients of the cation and anion, respectively.<sup>38</sup>

$$\Delta V = -\frac{eN\kappa}{\sigma\eta} \left[ \frac{D_+}{D_{0+}} - \frac{D_-}{D_{0-}} \right] \Delta P \quad (7)$$

In the present model, mechanical stress creates a fluid flow (convective flux) that drives ionic movement and induces charge separation due to differences in ion mobility.<sup>38</sup> Unlike the streaming model (eqn (2)), the latter approach considers not only fluid-driven ion transport, but also the different mobilities of individual ions. As a result, the dominant ion (the most mobile) drives the voltage generation with respect to the diffusion coefficients, which in turn depend on ion size, matrix porosity, permeability, and ion–matrix interactions. Therefore, a larger fluid flow speed and larger mobility difference between the ions produce a higher output voltage.<sup>38</sup> Wang *et al.*<sup>52</sup> proposed a different model based, this time, on the modified PNP (eqn (5)) coupled with Darcy's law (eqn (6)), yielding eqn (8):

$$\nabla V = \frac{c_i \frac{-\kappa}{\eta} \Delta P - a^3 D_i \nabla \cdot \left( \frac{c_i \nabla (c_+ + c_-)}{1 - a^3 c_+ - a^3 c_-} \right)}{\frac{e_0}{k_B T} z_i c_i} \quad (8)$$

While the previous model considered the spacing of ions and ion–ion interactions, the latter equations (eqn (7) and (8)) have been successfully applied to ion-pair systems, appropriately predicting their voltage generation.<sup>52</sup>

## Sensor composition and structural design factors affecting piezooionic performance

Piezooionic transducers operate by mechanically stimulating a polymer matrix or a gel, which generates a fluid pressure gradient that, in turn, drives ion flow within the matrix. As a result, a transient separation between the cations and anions takes place due to their different mobilities and interaction, breaking electrical neutrality and generating a transient voltage.<sup>38,39</sup> Thus, the polymer matrix and the ions are among the key factors influencing the performance of a piezooionic sensor. Structural parameters, such as the type of polymer matrix, its dimensions, the nature and mobility of the ions, the presence of liquid ion transporters, the charge density, the crosslinking density, porosity, microphase separation, and the introduction of a predetermined gradient of ions, significantly affect fluid-driven ion transport (Fig. 3). In the following sections, we will examine and analyse each of these structural parameters in detail. Unfortunately, unlike to the well-established measurement of ionic conductivity or the cycling of batteries, there is no common practice for the assembly and testing of piezooionic sensors. This makes the comparison of the results and performance analysis of the reported sensors quite a challenging task. Thus, we propose evaluating their performance based on the generated voltage range and the levels of applied pressure or strain forces. The key considerations include the maximum generated voltage, which facilitates future sensor applications, and the minimum applied force, which determines the device's sensitivity. These performance parameters are summarized in Table 2. Another important parameter for evaluating sensor performance is the response speed, or relaxation time, that is, the time required for the sensor to return to its initial state and become ready to generate a new response. However, the majority of reported studies have concentrated on the dependence of generated voltage on the applied mechanical force, whereas only a limited number have examined repeated cycling, which is necessary for assessing the relaxation time. Consequently, this parameter was not considered in this current review. As a result, piezooionic sensors can be categorized as follows:

### Type of polymer matrix and ionic species

The known piezooionic sensors can be categorized into the five groups based on the type of polymer matrix used:

#### I. Neutral polymers with ionic liquids (Table 2, entries 1–8).

The first group consists of commercially available neutral polymers doped with ionic liquids (ILs). Poly(vinylidene fluoride-hexafluoropropylene) (PVDF-HFP)<sup>46,54</sup> and thermoplastic polyurethanes (TPU)<sup>55–59</sup> are the most commonly used matrices due to their ability to form tough, elastic films, even at high filler loadings that exceed the polymer mass. These sensors contain both mobile cations and anions, contributing to ion migration under mechanical stress. It is worth noting that 1-ethyl-3-methylimidazolium bis(trifluoromethylsulfonyl)imide (EMIm<sup>+</sup>TFSI<sup>–</sup>) and 1-ethyl-3-methylimidazolium tetrafluoroborate



Table 2 Polymeric ionic materials and their electromechanical performance of piezionic sensors

Composition of the sensor				Performance of the sensor				Ref.
Entry	Polymer matrix	Mobile ions	Electrodes	Generated voltage range (mV)	Applied mechanical stimulus range (kPa, N, %, ° or mm) <sup>a</sup>	Notes		
1	Neutral polymers with ionic liquids PVDF-HFP (55 wt%) <sup>f</sup>	EMIm <sup>+</sup> TFSI <sup>-</sup> (37 wt%) <sup>f</sup>	Cu	30–90	1.5–37.5 kPa	EtMePyrr <sup>+</sup> TFSI <sup>-</sup> was added to the matrix as ionic plastic crystals $\sigma = 3.0 \times 10^{-3}$ S cm <sup>-1d</sup>	46	
2	PVDF-HFP (77 wt%) <sup>f</sup>	EMIm <sup>+</sup> TFSI <sup>-</sup> (20 wt%) <sup>f</sup>	Ag nanowires	20–95	10°–60° <sup>b</sup>	Microphase separated <sup>e</sup> Sensor possessed bilayer configuration $\sigma = 5.8 \times 10^{-7}$ S cm <sup>-1d</sup>	54	
3	TPU	EMIm <sup>+</sup> TFSI <sup>-</sup>	RGO/CNT/Ag	0.5–2.0	0.3–0.7% <sup>b</sup>	Gradient structure <sup>e</sup>	55	
4	TPU	EMIm <sup>+</sup> TFSI <sup>-</sup>	Graphene	0.5–4.5	0.4–1.6% <sup>b</sup>		55	
5	TPU (40 wt%) <sup>f</sup>	U <sup>c</sup> (60 wt%) <sup>f</sup>	MXene	21.0–290	0.6–1.3% <sup>b</sup>		56	
6	TPU (15.3 wt%) <sup>f</sup>	EMIm <sup>+</sup> TFSI <sup>-</sup> (76.1 wt%) <sup>f</sup>	Au/IITO glass	1.0–2.5	Max 10 kPa		57	
7	TPU (50 wt%) <sup>f</sup>	EMIm <sup>+</sup> BF <sub>4</sub> <sup>-</sup> (50 wt%) <sup>f</sup>	MXene/Ag	1.5–11	0.3–0.7% <sup>b</sup>	Lowest detectable pressure was not reported	58	
8	TPU	EMIm <sup>+</sup> TFSI <sup>-</sup>	H-reduced graphene oxide (RGO)/carbon nanotubes (CNTs)/Ag	0.6–2.6	0.3–1.8% <sup>b</sup>		55	
9	Neutral hydrogels with metal salts PVDF-HFP (95 wt%) <sup>f</sup>	Li <sup>+</sup> TFSI <sup>-</sup> (5 wt%) <sup>f</sup>	Cu	2.5–15	0.2–0.8 N	LiTFSI/propylene carbonate solution $\sigma = 1.0 \times 10^{-3}$ S cm <sup>-1d</sup>	40	
10	Crosslinked PAAm	Na <sup>+</sup> Cl <sup>-</sup>	PEDOT:PSS	0–0.6	0–100 kPa	Crosslinked using methylene bisacrylamide (MBA) and poly(ethylene glycol) diacrylate (PEGDA)	42	
11	Crosslinked PAAm/AMPS	Na <sup>+</sup> Cl <sup>-</sup>	Cu	8–150	12.25–36.75 kPa	Crosslinked using methylene bisacrylamide (MBA) and poly(ethylene glycol) diacrylate (PEGDA)	45	
12	PAAm/PVA (61.6 wt%) <sup>f</sup>	K <sup>+</sup> Fe[CN] <sub>6</sub> <sup>3-</sup> /K <sup>+</sup> Fe[CN] <sub>6</sub> <sup>4-</sup> Na <sup>+</sup> Cl <sup>-</sup> (38.4 wt%) <sup>f</sup>	PEDOT:PSS	6–700	1.4–20 N	$\sigma = 8.00 \times 10^{-2}$ S cm <sup>-1d</sup> Conductive pathways <sup>e</sup>	52	
13	Crosslinked PAAm/PVDF-HFP	Na <sup>+</sup> Cl <sup>-</sup> Li <sup>+</sup> Cl <sup>-</sup> Ca <sup>2+</sup> Cl <sup>-</sup> Li <sup>+</sup> Cl <sup>-</sup>	Cu	4–600	3 N	Crosslinked using methylene bisacrylamide (MBA) Porous/microphase separated <sup>e</sup>	60	
14	Crosslinked PAAm/AMPS		Au-plated Cu	1.8–27.3	30–150 kPa	Crosslinked using methylene bisacrylamide (MBA) Gradient structure <sup>e</sup>	61	
15	Polyelectrolyte ion gels with ionic liquids Nafion	EMIm <sup>+</sup> TFSI <sup>-</sup>	Au	0.1–1.3	0.1–1.6% <sup>b</sup>		56	
16	Nafion	EMIm <sup>+</sup> TFSI <sup>-</sup>	PEDOT:PSS	0.3–2.9	0.5–3.0% <sup>b</sup>	$\sigma = 1.4 \times 10^{-5}$ S cm <sup>-1d</sup>	62	
17	PAAm- <i>co</i> -PAA (50 wt%) <sup>f</sup>	H <sup>+</sup> (50 wt%) <sup>f</sup>	Au	0.4–2.8	60–350 kPa	15 wt% poly(acrylic acid- <i>co</i> -acrylamide) in DI water (AA:AAm = 50:50)	38	
18	Crosslinked PAA (40 wt%) <sup>f</sup>	H <sup>+</sup> Li <sup>+</sup> Cl <sup>-</sup> (59.9 wt%) <sup>f</sup>	Cu	0–30	17.4–319.16 kPa	Crosslinked using methylene bisacrylamide (MBA)	41	
19	Crosslinked gelatin-methacrylate/SPA	K <sup>+</sup>	Pt	0–35	1–50%	Crosslinked using methylene bisacrylamide (MBA) $\sigma = 4.34 \times 10^{-4}$ S cm <sup>-1d</sup>	43	
20	Crosslinked gelatin-methacrylate/ETA	Cl <sup>-</sup>	Pt	0–15	0–120 kPa 1–50%	Crosslinked using methylene bisacrylamide (MBA) $\sigma = 2.09 \times 10^{-4}$ S cm <sup>-1d</sup>	43	



Table 2 (continued)

Entry	Composition of the sensor				Performance of the sensor	Ref.
	Polymer matrix	Mobile ions	Electrodes	Applied mechanical stimulus range (mV) (kPa, N, %, °, or mm) <sup>a</sup>		
21	Crosslinked PAAm/SPA (23.1 wt%) <sup>f</sup>	K <sup>+</sup> (76.9 wt%) <sup>f</sup>	Pt	0–70 1–22.5 kPa	Crosslinked using methylene bisacrylamide (MBA) $\sigma = 1.05 \times 10^{-3}$ S cm <sup>-1</sup> <sub>d</sub> Gradient structure <sup>e</sup>	43
22	Crosslinked PAAm/AETA (26.5 wt%) <sup>f</sup>	Cl <sup>-</sup> (73.7 wt%) <sup>f</sup>	Pt	0–70 1–22.5 kPa	Crosslinked using methylene bisacrylamide (MBA) $\sigma = 7.11 \times 10^{-4}$ S cm <sup>-1</sup> <sub>d</sub> Gradient structure <sup>e</sup>	43
Solid-state polyelectrolytes						
23	Nafion	H <sup>+</sup>	Au	1.5–3.5 25–40	0.5–1.4% <sup>b</sup> 1.0–1.6% <sup>b</sup>	63
24	Nafion	H <sup>+</sup>	Au		Au electrode was deposited on polymer with specific tree-root-like structures	64
25	Nafion	H <sup>+</sup>	Graphdiyne	28–116	The ultrafast out-of-plane ion transfer was facilitated by the triangular pores in the graphdiyne electrodes	65
26	PEO/PIL (60 wt%) <sup>f</sup>	TFSI <sup>-</sup> (40 wt%) <sup>f</sup>	PEDOT:PSS	0.1–0.4 0.2–1 mm <sup>b</sup>	Ionic semi-interpenetrated network was used as matrix $\sigma = 8.7 \times 10^{-5}$ S cm <sup>-1</sup> <sub>d</sub>	66

<sup>a</sup> Mechanical stimulus is either pressure in kPa, force in N, strain in %, bending angle in ° or displacement in mm. <sup>b</sup> Piezoinionic sensors were tested in bending configuration. <sup>c</sup> Ionic liquid unspecified. <sup>d</sup> Ionic conductivity at 25 °C for some reported materials. <sup>e</sup> Morphological features. <sup>f</sup> Chemical composition of the top-performing piezoinionic sensor (ionic moiety and neutral backbone weight, %).

(EMIm<sup>+</sup> BF<sub>4</sub><sup>-</sup>) are among the most commonly used ILs due to their high ionic conductivity, as well as their exceptional thermal and electrochemical stability.

#### II. Neutral hydrogels with metal salts (Table 2, entries 9–14).

The most commonly used hydrogels are based on water-soluble polyacrylamide (PAAm) matrices crosslinked with bisacrylamide or with various poly(ethylene glycol) diacrylates (PEGDA).<sup>40,42,45,52,60,61</sup> To improve their mechanical stability in the swollen state, some linear polymers, such as poly(vinyl alcohol) (PVA) or PVDF-HFP were incorporated into a cross-linked PAAm network, forming semi-interpenetrating structures.<sup>52,55</sup> Following synthesis, these crosslinked polymers were impregnated with aqueous solutions of different metal salts, including NaCl, LiCl, KCl, K<sub>4</sub>[Fe(CN)<sub>6</sub>], K<sub>3</sub>[Fe(CN)<sub>6</sub>] or CaCl<sub>2</sub>.<sup>42,45,52,60,61</sup>

**III. Polyelectrolyte ion gels with ionic liquids (Table 2, entries 15 and 16).** The third group comprises polyelectrolyte-based sensors filled with ILs, with Nafion and its analogs being the most frequently used materials.<sup>56,62</sup> Since anions are chemically bonded to the polyelectrolyte backbone, a stable ion concentration gradient is formed within the polymer matrix under an applied force, which is supposed to further enhance the piezoinionic response.

**IV. Polyelectrolyte hydrogels (Table 2, entries 17–22).** This class of polymer matrices is typically synthesized by crosslinking ionic monomers, either cationic or anionic, with multifunctional neutral crosslinkers in an aqueous solution.<sup>38,41,43,44</sup> Commonly employed ionic monomers include [2-(acryloyloxy)-ethyl]trimethylammonium chloride (AETA), 3-sulfopropyl acrylate potassium salt (SPA),<sup>43,44</sup> and acrylic acid (AA),<sup>38,41</sup> which provide mobile counterions, such as chloride (Cl<sup>-</sup>), potassium (K<sup>+</sup>), or protons (H<sup>+</sup>). To obtain hydrogels with controlled sizes and complex geometries, 3D printing techniques have been successfully applied, as demonstrated by Odent *et al.*<sup>43,44</sup> Notably, these polyelectrolyte hydrogels typically contain only a single type of mobile ionic species, which simplifies the generation of ion gradients under applied mechanical deformation.

**V. Solid-state polyelectrolytes (Table 2, entries 23–26).** The final category comprises fully solid-state sensors constructed exclusively from charged polymers, either anionic<sup>63–65</sup> or cationic<sup>66</sup> polyelectrolytes. Among polymers bearing covalently bound anions, the commercially available Nafion has been frequently employed.<sup>63–65</sup> In other studies, anionic or cationic ionic liquid-like monomers (ILMs) were selected as precursors, as their polymerization yields poly(ionic liquid)s (PILs) with inherently high ion mobility, a key factor for efficient sensor response. A major challenge in PIL-based systems is balancing the ionic conductivity (ion mobility) with mechanical robustness (viscoelastic properties). To address this, Ribeiro *et al.*<sup>66</sup> involved the design of semi-interpenetrating networks (semi-IPNs) combining a linear conductive PIL with a reinforcing polyethylene oxide matrix, specifically a synergistic composition was achieved with better mechanical properties and ionic conductivity compared with its individual components.

#### Single-ion vs. ion-pair mobility

The five categories mentioned can be further classified into two large classes: systems where both cations and anions are

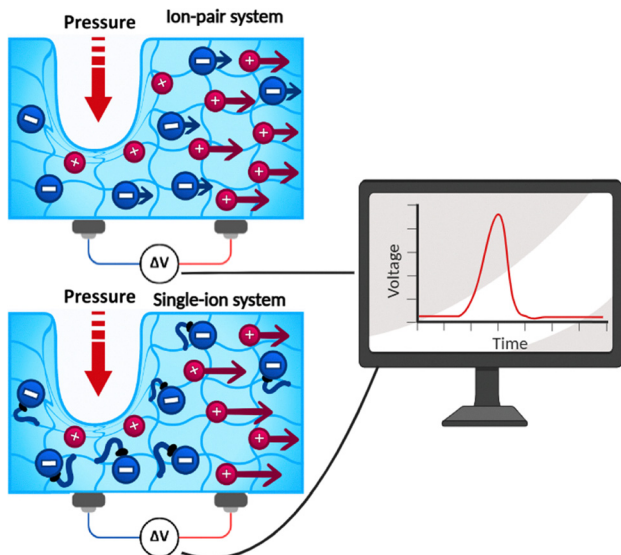


Fig. 4 Mechanical-to-ionic transduction of the single-ion and ion-pair based ionic materials, leading to transient voltage generation with respect to the transient separation of anionic and cationic species in response to an applied mechanical load.

mobile (I–III, ion-pair mobility) and systems with only a single mobile ion (IV–V, single-ion mobility), as illustrated in Fig. 4. In the systems containing two mobile ionic species (metal salts or ILs), the mechanical-to-ionic transduction is dictated by the transient charge separation caused by the strain-driven ion flux and the preferential displacement of the cations over the anions, and *vice versa*. Enlarging the difference in mobility between the anions and cations results in an amplified ionic gradient, thereby generating an enhanced voltage response. In this context, an enhanced voltage response is typically observed in systems where the polymer matrix is modified to either selectively facilitate or hinder ion migration. Such modifications (Table 2, entries 1, 2 and 6) give rise to ion-selective transport, driven by specific ion–matrix interactions.<sup>46,54,58</sup> For instance, Lee *et al.*<sup>58</sup> showed that incorporating EMIm<sup>+</sup> TFSI<sup>−</sup> ionic liquid into a TPU matrix resulted in a cation-driven piezoionic response (Table 2, entry 6). This behavior was attributed to stronger ion–dipole interactions between the TPU matrix and the TFSI<sup>−</sup> anion, rendering EMIm<sup>+</sup> more mobile than TFSI<sup>−</sup>. Similarly, Weiyan *et al.*<sup>46</sup> utilized a PVDF–HFP matrix for enhancing TFSI<sup>−</sup> mobility; strong dipole interactions preferentially immobilized EMIm<sup>+</sup> (Table 2, entry 1). When different EMIm-based ILs were incorporated into a TPU matrix (Table 2, entries 3–8), the generated voltage remained low, regardless of the electrode type. Sensors with EMIm<sup>+</sup> TFSI<sup>−</sup> produced voltages in the range of 0.5–4.5 mV,<sup>55,56,58</sup> whereas replacing TFSI<sup>−</sup> with the BF<sub>4</sub><sup>−</sup> anion (EMIm<sup>+</sup> BF<sub>4</sub><sup>−</sup>) increased the response up to 11 mV.<sup>59</sup> This enhancement can be attributed to the smaller size of BF<sub>4</sub><sup>−</sup>, which increased the relative mobility difference between BF<sub>4</sub><sup>−</sup> and EMIm<sup>+</sup> under the same strain. More generally, it can be speculated that the limited performance of TPU-based systems can result from the hard segments of the TPU chains, which restrict ion mobility and

thus suppress voltage generation. In contrast, when EMIm<sup>+</sup> TFSI<sup>−</sup> was embedded in a PVDF–HFP matrix (Table 2, entries 1 and 2), the sensors displayed significantly superior piezoionic responses.<sup>46,54</sup> Remarkably, output voltages of 90–95 mV were reported, representing a substantial improvement over TPU-based systems. This enhanced performance can be attributed not only to the use of PVDF–HFP, but also to specific structural features embedded within these sensors. Even when EMIm<sup>+</sup> TFSI<sup>−</sup> was replaced with the less conductive LiTFSI propylene carbonate solution (Table 2, entry 9),<sup>40</sup> and PVDF–HFP was used without additional structural modifications, the resulting sensor still outperformed the TPU-based congeners, generating voltages of up to 15 mV. However, switching from neutral polymers to charged Nafion filled with EMIm<sup>+</sup> TFSI<sup>−</sup> (Table 2, entries 15 and 16) did not lead to a significant improvement in output voltage, regardless of the electrode type.<sup>56,62</sup> This limitation is likely due to ionic interactions and ion-exchange processes involving the covalently bound SO<sub>3</sub><sup>−</sup> groups, H<sup>+</sup> counterions, and the EMIm<sup>+</sup> TFSI<sup>−</sup> ion pairs. Such interactions likely restricted ion mobility in response to mechanical stress, thereby diminishing the mechanical-to-ionic transduction.

Single-ion conducting matrices (Table 2, 17–26) are particularly attractive for piezoionic sensing, as they are expected to promote a relatively strong and stable ion-gradient formation under mechanical stress. Compared with ion-pair systems, single-ion systems offer distinct advantages, most notably the ability to differentiate between transient and static loads.<sup>38,44</sup> Under a transient mechanical stimulus, the applied stress induces a voltage that relaxes once the load is released, resulting in a transient recovery. By contrast, a static load leads to a gradual reduction of the fluid pressure gradient, slowing down fluid flow and causing voltage decay over time.<sup>38</sup> In ion-pair systems, this effect is exacerbated because the imbalance between cation and anion distributions is inherently short-lived,<sup>39</sup> leading to significant voltage loss. However, the charge separation persists over longer timescales, thereby reducing voltage decay and enabling more reliable sensing performance. Finally, the performance of single-ion conducting systems strongly depends on the mobility of the free ions. This mobility is influenced by multiple factors, including the type of anions and cations, the nature and length of the spacer between the polymer backbone and the covalently bound ion, the type of crosslinker, and the presence of specific interactions between the polymer matrix and the mobile ions. For a more detailed discussion of these factors, readers are referred to recent reviews on PILs.<sup>67,68</sup> Considering all the advantages of gradient ion distribution under mechanical load in single-ion conducting matrices, it was anticipated that well-designed polymer matrices would enable sensors with excellent performance. A notable example is system based on Nafion (Table 2, entry 25)<sup>65</sup> which delivered some of the highest output voltages among the cases summarized in Table 2. Even when polyelectrolytes were combined with relatively less mobile ions, such as K<sup>+</sup> and Cl<sup>−</sup> (compared with H<sup>+</sup>, BMIm<sup>+</sup>, or TFSI<sup>−</sup>), their formulation as hydrogels allowed water to act as an ion



transporter, enabling the generation of voltages as high as 70 mV under a 22.5 kPa load.<sup>44</sup>

### Hydrogels/ionogels vs. solid-state systems

When it comes to hydrogels and organogels,<sup>38–45,52,60,61</sup> both the magnitude and response speed of the generated voltage depend not only on the transport of mobile ions, but also on the movement of solvent molecules and solvated ion-pairs.<sup>69</sup> On one hand, the presence of water as an ion transporter greatly facilitates ion mobility, leading to unprecedented levels of ionic conductivity and in turn enables an ultrafast response and exceptionally high voltage output (Table 2, entries 11–13).<sup>45,52,60</sup> Although direct comparison is complicated by differences in assembly and testing methodologies, both neutral polymers (Table 2, entries 11–13)<sup>45,52,60</sup> and polyelectrolytes (Table 2 entries 21 and 22)<sup>44</sup> when swollen in water or aqueous salt solutions were able to deliver high sensitivity and strong voltage responses. Since water readily evaporates, it has been partly substituted with the less volatile glycerol (Table 2, entries 21 and 22).<sup>44</sup> This modification yields ionically conductive gels with enhanced stability under open-air conditions, while still achieving output voltages of up to 70 mV under a 22.5 kPa load. However, despite these impressive sensing performances, solvent evaporation remains a major limitation for the practical application of such systems in sensors. Unlike hydrogels or organogels, ionogels (Table 2, entries 15 and 16) are inherently non-volatile, as ionic liquids possess nearly zero vapor pressure.<sup>56,62</sup> Consequently, the incorporation of ionic liquids imparts non-volatility and outstanding thermal stability.<sup>46,54–59</sup> Still, a major drawback of these systems is the potential leaching of ionic liquids from the polymer matrix under mechanical stress, which poses a significant risk to long-term performance. The presence of ion transporters, such as water, glycerol, or ILs, within the polymer matrix significantly enhances sensor performance. Hydrogel-based polymeric ionic materials, in particular, have demonstrated outstanding results, generating voltages of up to 600–700 mV under loads of 3–20 N (Table 2, entries 12 and 13),<sup>52,60</sup> a record among the reported values in Table 2. Notably, neutral hydrogels containing metal salts generally exhibited higher performance (Table 2, entries 11–13)<sup>45,52,60</sup> compared to polyelectrolyte hydrogels (Table 2, entries 18–22).<sup>41,43,44</sup> This difference can be attributed to variations in sensor assembly (see section Operating Parameters) and the types of ions employed.

Solid polymer electrolytes provide improved safety compared to hydrogels or ionogels, as they eliminate the risks of leakage, evaporation, or leaching associated with liquid phases. The absence of a liquid component is particularly critical for skin- and health-monitoring sensors, ensuring long-term stability, biocompatibility, and reliable performance under continuous wear. These factors have stimulated a growing trend toward the development of solid-state piezooionic sensors (Table 2, entries 23–26).<sup>63–66</sup> It is particularly important to emphasize the critical role of polymer matrix design in this case. By carefully selecting optimal parameters, such as highly mobile ions, the nature of the polymer backbone, crosslinking

density, strong interfacial contact with the electrode material, and the use of elastic electrodes, the solid-state systems can provide strong competition with hydrogels. As seen from the solid-state systems (Table 2, entry 25), they can deliver responses of up to 116–190 mV, ranking as the third- and fifth-highest results among all the piezooionic sensors reported.

### Ion mobility

Ion mobility depends on the diffusion of ions within the matrix, which in turn depends on the ion's electronic charge, size, concentration, and electrophoretic mobility.<sup>38,39,44</sup> According to the Stokes–Einstein equation (eqn (9)), where  $D_i$  is the diffusion coefficient of ion  $i$ ,  $k_B$  is the Boltzmann constant,  $T$  is the absolute temperature,  $\eta$  is the viscosity, and  $r_i$  is the hydrodynamic radius of the ion,<sup>70</sup> larger ions would experience higher viscous drag force compared with smaller ions, thus decreasing the diffusion of ions within the direction of the fluid flow as follows:

$$D_i = \frac{k_B T}{6\pi\eta r_i} \quad (9)$$

This difference is well illustrated by comparing TPU-based systems incorporating  $\text{EMIm}^+$   $\text{TFSI}^-$ <sup>55,56,58</sup> and  $\text{EMIm}^+$   $\text{BF}_4^-$ <sup>59</sup> ionic liquids (Table 2, entries 3, 4, 6 and 7). While the cation remains the same, the  $\text{BF}_4^-$  anion is considerably smaller than  $\text{TFSI}^-$ , which enables higher ion mobility and, consequently, improved sensor performance. According to the Nernst–Einstein equation (eqn (10)) where  $\mu_{qi}$  is ionic mobility of ion  $i$ ,  $D_i$  is the diffusion coefficient of ion  $i$ ,  $k_B$  is the Boltzmann constant,  $T$  is the absolute temperature,  $z_i$  is the electron valence of ion  $i$ ,  $e$  is the fundamental charge,<sup>70</sup> the migration of ions is also under the influence of a transient electrical field during charge separation, referred to as the electrophoretic mobility, reducing ion transport within the direction of the fluid flow as follows:

$$\mu_{qi} = \frac{q_i D_i}{k_B T} = \frac{z_i e D_i}{k_B T} \quad (10)$$

Although ion–matrix, ion–ion, and ion–solvent interactions are not considered, the combination of eqn (9) and (10) leads to eqn (11), showing that the charge-to-ion size ratio clearly defines the ionic mobility.<sup>70</sup>

$$\mu_{qi} = \frac{z_i e}{6\pi\eta r_i} \quad (11)$$

As a result, the total migration flux of an ion is mainly due to the convection flow, whereas the viscous flow (with respect to concentration gradient; diffusive flow) and the electrophoretic flow (with respect to the charge gradient) drive the migration of ions in a reverse direction, causing voltage decay.<sup>38</sup>

### Material dimensions

Material dimensions like the material thickness affect the pressure distribution along the polymeric matrix. Specifically, the lower the material thickness, the higher the generated voltage and the response speed with respect to narrow force distribution, upon mechanical deformation.<sup>38,45,46</sup>



Poroelasticity describes the time-dependent behavior of fluid-containing materials during mechanical loading.<sup>38</sup> Under mechanical stimulation, ions are transported with a fluid flow due to the generation of a pressure gradient, which subsides and redistributes within the material until the pressure is equilibrated. The characteristic time taken for a material to relax after deformation is applied is namely the poroelastic relaxation time, which is expressed as  $\tau = \frac{(1-2\nu)\eta L^2}{2(1-\nu)G\kappa} \sim \frac{L^2}{D}$ , where  $L$  is the characteristic length,  $\nu$  is the Poisson's ratio,  $G$  is the modulus,  $\eta$  is the fluid viscosity,  $\kappa$  is the material permeability and  $D$  is the effective diffusivity of the fluid, govern the piezionic recovery time.<sup>38,71,72</sup> As a result, longer poroelastic relaxation times result in a slower fluid flow, which in turn leads to longer recovery times.<sup>71,72</sup>

### Charge density, crosslinking density and material density

These are key parameters affecting the charge separation and the resulting output voltage with respect to the flow of charges within a material. Charge density herein refers to the number of mobile ions (or charge) per unit volume; hence, the higher the charge density, the higher the generated output voltage. In contrast, the crosslinking density corresponds to the degree of crosslink points per unit volume, leading to higher resistance to flow within a material. Herein, the generated amplitude of the output voltage at a given applied pressure is approximately proportional to the charge density and inversely proportional to the crosslinking density.<sup>44</sup> Dobashi *et al.*<sup>38</sup> attributed a slight attenuation in the amplitude of the output voltage together with longer recovery time to the material density, namely the mass of a material per its unit volume. The latter more effectively leads to changes in the material permeability (ability for fluids to flow through media) and stiffness (modulus).<sup>38,39</sup>

## Novel strategies for structural design towards enhanced piezionic performance

Recently, several novel strategies for structural design have been proposed for enhancing the performance of piezionic sensors. These include the introduction of porosity, microphase separation, gradient-like architectures, and the creation of conductive pathways or gates, as follows:

### Porosity

Porosity refers to the ratio of the void space inside the total volume in a material, and is generally obtained by means of solvent casting or porogen leaching.<sup>60,73</sup> Porosity directly influences the mechanical properties (stiffness) and the permeability of a material, which governs ion diffusion within a piezionic material (Fig. 5).<sup>38,45,60</sup> Consequently, porosity enhances the generated output voltage through two main mechanisms: (1) facilitating easier deformation (reduced stiffness), which increases electromechanical sensitivity, and (2) enhancing the dipole moment, which promotes more

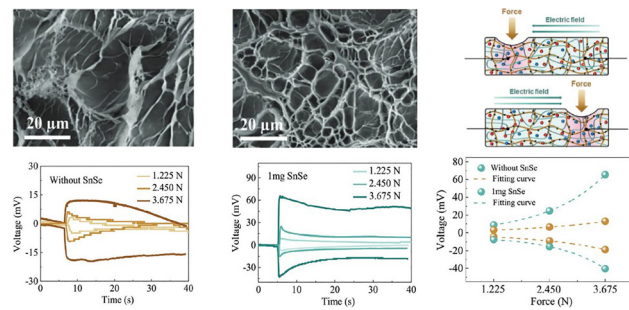


Fig. 5 Influence of porosity upon addition of tin selenide nanosheets (SnSe) within polymeric ionic materials with respect to higher generated output voltage. Reproduced with permission from *Adv. Funct. Mater.*<sup>45</sup>; © 2023 Wiley-VCH GmbH.

efficient charge separation.<sup>45,60</sup> Using double-network nanocomposites embedded with an electrolyte ( $\text{NaCl}$  or  $\text{K}_3\text{Fe}[(\text{CN})_6]/\text{K}_4\text{Fe}[(\text{CN})_6]$ ), Li *et al.*<sup>45</sup> demonstrated that smaller pore sizes led to larger mobility differences between the ions, thus allowing for a higher output voltage. Lu *et al.*<sup>60</sup> further demonstrated a three-fold increase in the output voltage (up to 14 mV under 3 N loading) from porous PAAm hydrogels embedded with electrolytes ( $\text{CaCl}_2$ ,  $\text{NaCl}$  or  $\text{LiCl}$ ) compared to their nonporous counterparts together with a higher output voltage with respect to the size of the hydrated ions:  $\text{Ca}^{2+}$  (4.12 Å) >  $\text{Li}^+$  (3.82 Å) >  $\text{Na}^+$  (3.58 Å) due to higher mobility imbalance (Table 2, entries 11 and 13).

### Microphase separation

Microphase separation is a phenomenon in which a material organizes into distinct domains.<sup>74</sup> This structural arrangement enables relatively high output voltage amplitudes under increased pressure gradients by concentrating stress within the hard phases, while simultaneously exploiting the high ionic mobility of the soft and intermediate phases (Fig. 6).<sup>46,60</sup> For example, Lu *et al.*<sup>60</sup> combined microscopic porosity and hydrophilic-hydrophobic phase separation into electrolyte-loaded PAAm networks for pronounced piezionic performance, generating output voltages as high as 600 mV in response to a medical ultrasound stimulation (Table 2, entry 13). Additionally, Zhu *et al.*<sup>46</sup> introduced  $\text{EMIm}^+$   $\text{TFSI}^-$  ionic liquid as a compatibilizer within a microphase-separated system based on ionic plastic crystals and PVDF-HFP for stress concentration and localized charge separation, yielding improved mechanical properties and effective voltage generation up to 90 mV under a 15 kPa loading.

### Gradient-like structures

Gradient-like structures refer to materials with gradually varying properties along their volume (Fig. 7).<sup>75</sup> Odent *et al.*<sup>44</sup> developed such polyelectrolyte hydrogels through the copolymerization of AAm with either anionic 3-sulfopropyl acrylate potassium salt (SPA) or cationic [2-(acryloyloxy)ethyl]trimethylammonium chloride (AETA) co-monomers (Table 2, entries 20 and 21). This was achieved using the stereolithography 3D printing of stacked ionic assemblies composed of discrete



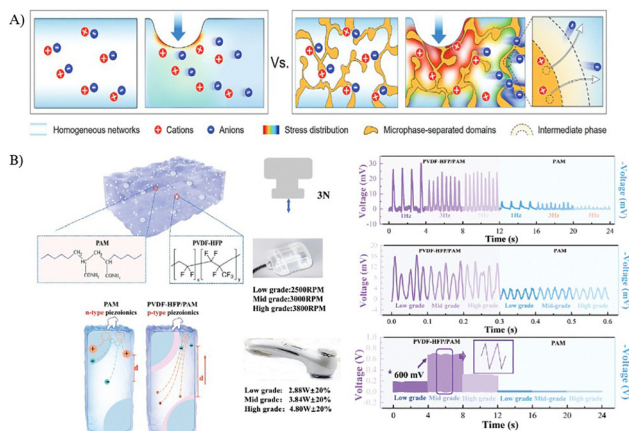


**Fig. 6** Influence of microphase separation within polymeric ionic materials with respect to higher stress localization and enhanced ion separation in comparison to homogeneous networks (A). Reproduced with permission from *Adv. Mater.*<sup>46</sup>, © 2024 Wiley-VCH GmbH. Microphase-separated PAAm/PVDF-HFP leads to higher transient voltage generation compared to homogeneous PAAm network with respect to higher ion mobility difference (B). Reproduced with permission from *Adv. Mater.*<sup>60</sup>, © 2023 Wiley-VCH GmbH.

compartments with distinct ion transport properties. By varying the ion type, charge density, and crosslinking density across these compartments, the output voltage magnitude and polarity of the resulting piezoelectric device could be precisely programmed (Fig. 7A). The generated voltage at a given applied pressure was found to be directly proportional to the hydrogel's charge density and inversely proportional to its crosslinking density. Gradient-like structures leverage this principle and allow for the programming of the signal magnitude, enabling

controlled amplification or attenuation, through the flow of excess charges from the indented compartment to adjacent compartments with different ion transport properties. As a result, the resulting touch sensors can be integrated onto fingertips, enabling a tactile perception for object recognition applications. Recently, Li *et al.*<sup>61</sup> dramatically enhanced the piezoelectric outputs of LiCl-embedded PAAm hydrogels by leveraging the synergistic effects among geometry, modulus (stiffness), and charge gradients (Table 2, entry 14). While the geometry and modulus gradients enhanced the generation of a pressure gradient, the charge gradient increased the mobility difference between the ions, thus leading to a higher output voltage (Fig. 7B). Similarly, Kim *et al.*<sup>54</sup> (Table 2, entry 2) developed bilayer-structured polymeric ionic materials that exhibited a significantly enhanced output signal and faster response time due to the presence of an ion accumulation interface (Fig. 7C). The material further demonstrated the capability to accurately detect both static and dynamic forces, including specific motions, such as bending and vibrations.

### Conductive pathways and gates

Conductive pathways and gates can boost the transport of ions within a material, thus improving its piezoelectric performance. Dai *et al.*<sup>41</sup> (Table 2, entry 18) introduced oriented polyethylene terephthalate (PET) fibers into LiCl-embedded polyacrylic acid to create conductive pathways that facilitated ion transport along the negatively charged fiber surfaces (Fig. 8). As a result, the output voltage measured parallel to the fiber orientation was significantly higher (27.5 mV vs. 4.3 mV under a 290 kPa load) and exhibited a much faster recovery time (1.5 s vs. 30 s) compared to that in the perpendicular direction. Wang *et al.*<sup>52</sup>

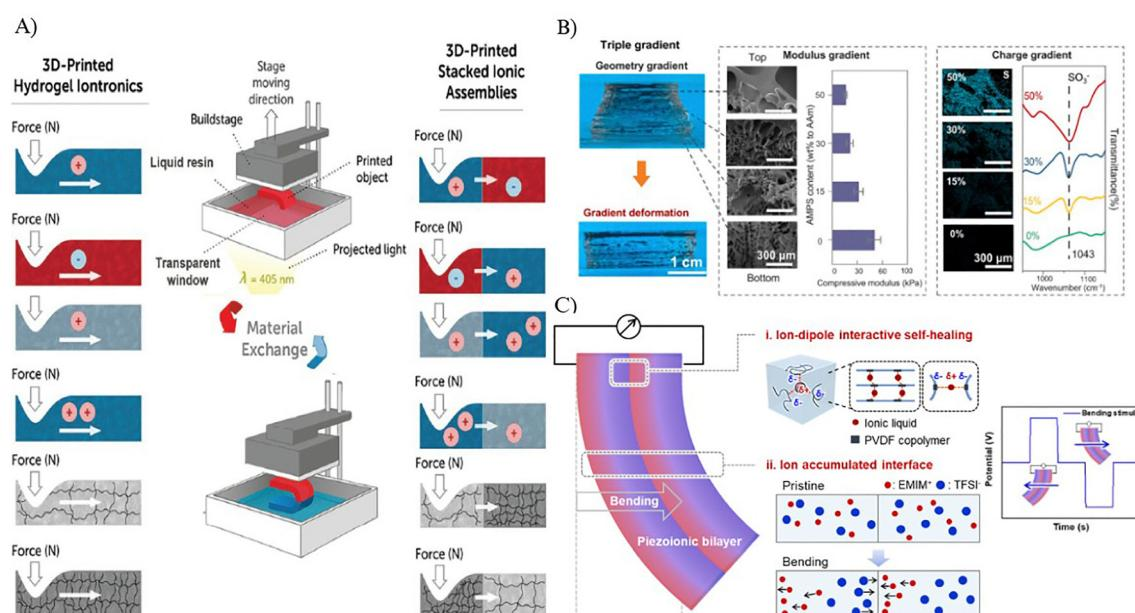


**Fig. 7** Gradient-like structures by means of variations in ion type, charge density, and crosslinking density within the piezoelectric device via resin vat exchange during 3D printing (A). Reproduced with permission from *Adv. Funct. Mater.*<sup>44</sup>, © 2022 Wiley-VCH GmbH. Multi-gradient structures combining geometry, modulus (stiffness), and charge gradients (B). Reprinted with permission from *Nano Energy*<sup>61</sup>, © 2024 Elsevier Ltd. Bilayer polymeric ionic materials with enhanced piezoelectric performance with respect to an ion accumulation interface (C). Reprinted with permission from *Nano Energy*<sup>54</sup>, © 2024 Elsevier Ltd.



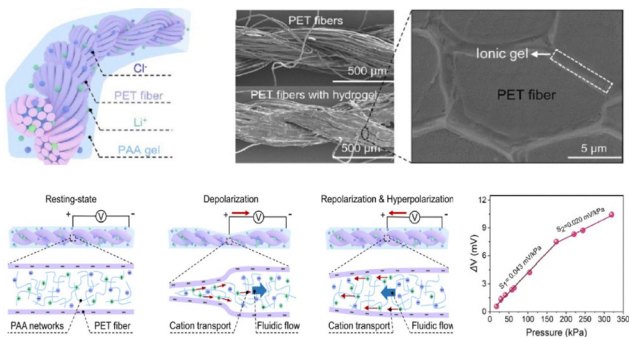


Fig. 8 Conductive pathways by oriented PET fibers within piezoionic materials, providing higher mechanical-to-ionic transduction and resulting voltage generation along the fiber directions. Reprinted with permission from Device<sup>41</sup>; © 2024 Elsevier Inc.

(Table 2, entry 12) employed a combination of PAAm, polyvinyl alcohol (PVA), and poly(3,4-ethylenedioxythiophene):poly(styrenesulfonate) (PEDOT:PSS) followed by a simple dry-annealing process to induce a gating effect. Under high pressure, this effect resulted in the accumulation of anions within the indented region. The resulting gate remained open under low deformation, but progressively closed once a threshold force was exceeded. Mechanistically, PEDOT forms crystalline aggregates through  $\pi$ - $\pi$  stacking, which undergo oxidation, creating a conductive polymer network. This network contains excess positive charges (holes) that electrostatically interact with anions embedded in the hydrogel, thereby reducing their diffusivity.<sup>52</sup> In contrast, PSS with its negatively charged sulfonate groups forms ordered nanostructures that act as pathways for embedded cations to move within the hydrogel.<sup>52</sup>

## Unveiling operating parameters for piezoionic voltage generation

The operating parameters associated with the sensor configuration and assembly can significantly influence fluid-driven ion transport in piezoionic sensors (Fig. 9). In the following sections, we examine in detail the most critical of these parameters:

### Electrode configuration

The two-electrode configuration is the most widely adopted assembly scheme for piezoionic sensors, typically implemented in two modes: coplanar and bending. In the coplanar mode, two electrodes are positioned on the same surface of the material, which is subjected to a compressive stimulus. This drives ion flow and charge transport perpendicular to the indentation. When the reference (ground) electrode is placed beneath the indented region and the working (sensing) electrode on the undeformed region, the resulting voltage polarity can be interpreted based on the ion species that are preferentially displaced: a positive output indicates cation-driven transport, whereas a negative output indicates anion-driven transport (and *vice versa*).<sup>44</sup> By contrast, electrodes are placed

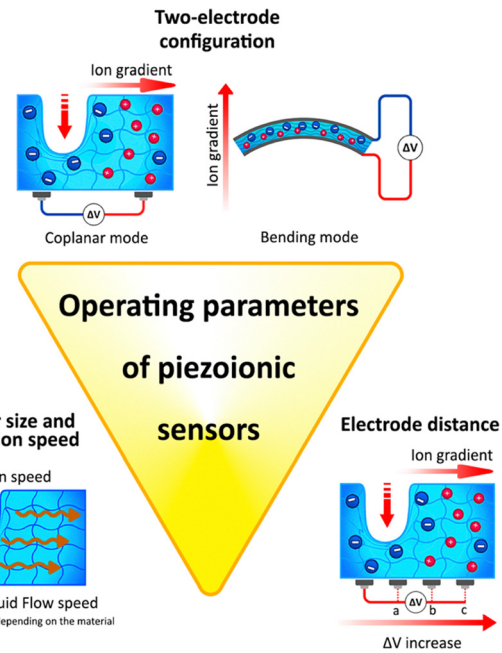


Fig. 9 Operating parameters affecting the fluid-driven ion transport and voltage generation in piezoionic sensors, including the electrode configuration, the electrode distance and the indentation characteristic (size and speed).

on opposite faces of the material in the bending mode, where bending deformation drives ion flow and charge transport parallel to the deformation. Ko *et al.*<sup>54</sup> suggested a bilayer-structured ionic materials for enhancing the output signal and the response time of the sensor, which was constructed after spraying silver nanowires on one side of a film and then half-cutting it; the two films were then assembled face-to-face (Table 2, entry 2).

### Electrode composition

Various electrode materials were investigated (Table 2), including metal electrodes such as Cu,<sup>40,41,45,60</sup> Au,<sup>38,62–64</sup> Ag,<sup>54</sup> reduced graphene oxide/carbon nanotubes/silver (RGO/CNT/Ag),<sup>55</sup> gold and indium tin oxide glass (Au/ITO glass),<sup>59</sup> graphene,<sup>56</sup> two-dimensional titanium carbide/silver (MXene/Ag)<sup>57</sup> and PEDOT:PSS.<sup>52,66</sup> The range of choices in electrode materials is limited by some challenges related to contact with elastic polymer films or hydrogels, and precise current collection. Vapor-phase deposition is primarily employed for sensors operating in compression mode, where a thin conductive layer, typically of noble metals, is directly coated onto polymer films or ionogels, providing excellent conductivity and signal retention.<sup>55,62,63</sup> Although noble metals have been widely used as electrodes, their poor mechanical compliance and limited stability under high deformation significantly restrict their effectiveness in bending-mode sensors, especially under large strains.<sup>55,62,76,77</sup> In the bending mode, the electrode selection plays a more decisive role in determining the generated voltage, largely due to interfacial challenges between polymeric ionic materials and electrodes.<sup>55,56,58,63,64</sup> To overcome these



limitations, more flexible and conductive alternatives, such as Ag nanowires,<sup>54</sup> graphene,<sup>56</sup> MXene,<sup>57,59</sup> graphdiyne,<sup>65</sup> and PEDOT:PSS<sup>42,52,62,66</sup> have been investigated (Table 2, entries 2, 4, 5, 7, 10, 12, 16, 25 and 26). For instance, Lu *et al.*<sup>56</sup> (Table 2, entry 5) developed a trilayer sensor based on a TPU matrix with ILs and MXene electrodes, demonstrating superior electromechanical transduction. The improved performance was attributed to the ultrathin MXene layers with a larger surface area and a higher pore distribution compared to the bulk MXene, yielding output voltages up to 219 mV with excellent cycling stability (98% retention after 10 000 cycles). In another study, Lu *et al.*<sup>65</sup> (Table 2, entry 25) reported a trilayer sensor composed of Nafion and graphdiyne electrodes, which facilitated rapid in-plane and out-of-plane ion transport. This design achieved a high output voltage of 116 mV, along with robust stability (94.7% signal retention after 4000 cycles). Similarly, conductive polymers, such as PEDOT:PSS impart stability, high conductivity, and excellent stretchability to polymeric sensors.<sup>42,52,57</sup> For example, Ribeiro *et al.*<sup>66</sup> (Table 2, entry 26) fabricated highly stretchable, ionically conductive films coated with flexible PEDOT:PSS electrodes on both sides. At low scan rates, these devices demonstrated volumetric capacitances equivalent to, or even exceeding, those of systems employing ionic liquid electrolytes.

### Electrode distance

The electrode spacing strongly influences both the magnitude of the output voltage and recovery time, as it determines the spatio-temporal variation of fluid flow that drives ion transport.<sup>39</sup> Under mechanical stimulation, a pressure gradient induces fluid flow, which carries ions and establishes a spatio-temporal electric field within the piezoionic device. Xu *et al.*<sup>39</sup> systematically investigated the effect of the electrode distance using both cationic and anionic single-ion based piezoionic sensors. They demonstrated that increasing the electrode distance led to higher output voltages, but also resulted in longer recovery times (Fig. 10). This behaviour can be explained by the spatial dependence of the electrical potential, described as  $V = \int E(x, t) dx$ , where  $V$  is the voltage,  $E$  is the electrical field,  $x$  is the distance between the electrodes and  $t$  is time. Consequently, a larger electrode distance results in a higher output voltage. In contrast, the longer the electrode distance, the greater the recovery time as a longer poroelastic relaxation pathway is required for the material to fully recover after deformation.<sup>39</sup>

### Indentation size and speed

The indentation size and speed play crucial roles in the generation of a pressure gradient during mechanical loading. Larger indentation sizes result in higher voltage outputs.<sup>44</sup> Additionally, Xu *et al.*<sup>39</sup> showed that increasing the indentation speed enhances both the output voltage and reduces the recovery time. However, the voltage response eventually saturates at high indentation speeds, reaching a plateau that reflects an optimal characteristic fluid flow velocity.<sup>39</sup> Similarly,

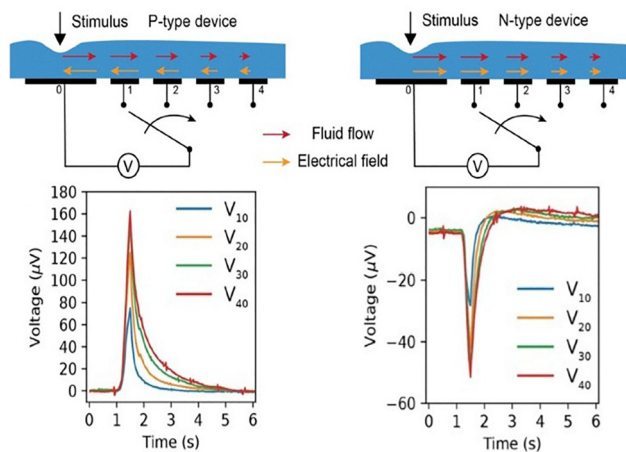


Fig. 10 Electrode distance effect on both cationically (P-type device) and anionically (N-type device) driven polymeric ionic material together with their respective output voltage as a function of time. Used with permission from *Mater. Horiz.*<sup>39</sup>; © 2024 The Royal Society of Chemistry.

the response and recovery times (FWHM) reach a plateau with further increases in the indentation speed. Dai *et al.*<sup>41</sup> consistently reported a comparable trend, observing an increased output voltage with faster indentation speeds.

### Applications

**Soft wearable electronics** are increasingly being employed for the continuous, non-invasive health monitoring of physiological parameters, offering improved disease diagnosis, progression tracking, and treatment at a relatively low cost.<sup>78,79</sup> Such electronics typically consist of a sensing unit combined with a data collection/transmission unit and a power supply.<sup>80</sup> Piezoionic systems are self-powered and highly sensitive to mechanical stimuli, making them suitable for telehealth applications. This requires the detection of subtle signals and continuous monitoring over extended periods, such as in the case of cardiac monitoring.<sup>65</sup> For example, cardiovascular monitoring, including heart rate and blood pressure monitoring, is crucial for the early detection of heart conditions and diseases.<sup>65</sup> In this regard, piezoionic sensors readily allow for the continuous monitoring of patient deterioration.<sup>78,79</sup> Lu *et al.*<sup>65</sup> developed a wearable piezoionic sensor capable of distinguishing between systolic and diastolic blood pressures, with measurements consistent with those of commercial devices. Ma *et al.*<sup>42</sup> introduced a dual piezoionic sensor for monitoring both the heart rate and sodium levels in sweat to provide heart parameter monitoring and homeostasis information. While others reported on piezoionic sensors for monitoring heart rate, blood pressure, and human motion,<sup>56,57,65</sup> piezoionic sensors have also been used for respiratory and sleep monitoring.<sup>56,57,65</sup>

**Ionic skins, tissue engineering, and biointerfaces** represent a promising avenue for the application of piezoionic sensors with respect to their biomimetic mechanical-to-ionic transduction mechanism, their ability to mimic the production of biological signals and their transmission.<sup>6-8</sup> Particularly, complex tactile



perception gives rise to the development of ionic-based systems able to mimic some of the functionalities of the skin, well-known as ionic skin.<sup>81</sup> Wang *et al.*<sup>52</sup> developed a piezoionic material able to discriminate between innocuous and harmful touch similar to skin receptors. Lu *et al.*<sup>60</sup> developed a piezoionic sensor able to differentiate the spatial localization of pressure. Tissue engineering is an interdisciplinary field that focuses on the restoration of damaged or diseased tissues, and requires biocompatible materials that allow for cell attachment, proliferation, and differentiation. Burattini *et al.*<sup>43</sup> proved the biocompatibility of gelatin-based, single-ion piezoionic systems with respect to cell proliferation and the differentiation of myoblasts, with no adverse effects. Biointerfaces are devices that interact with the neural system to treat a disorder or symptom.<sup>80,82</sup> In that regard, Dobashi *et al.*<sup>38</sup> demonstrated that the neuromodulation capabilities of a piezoionic system were able to elicit muscle excitation in mice. Lue *et al.*<sup>41</sup> developed an artificial nerve system using a composite of PET microfiber and PAAc hydrogel, which neuromodulated stimuli in the peripheral sciatic nerve of mice. This proved its capabilities to communicate and be integrated with biological nerve systems. In general, polymeric ionic materials for ionic skin, biointerfaces, neuromodulation or neuroprosthetics must generate an electrical potential of approximately 15–20 mV (threshold potential) to trigger an action potential, enabling communication within the body.<sup>6–10,38,41</sup> Focusing on ionic skin applications, piezoionic materials should be able to mimic the complex somatosensory system of the skin. Specifically, this includes mimicking the four low-threshold mechanoreceptors in the skin: Merkel cells, Meissner corpuscles, Pacinian corpuscles, and Ruffini endings. Firstly, the sensitivity of polymeric ionic materials to deformation should match the sensitivity of these mechanoreceptors in the skin, which can detect forces as subtle as 0.5 mN.<sup>6–8</sup> As such, Fig. 11 illustrates the maximum output potential against the frequency response time for selected piezoionic sensors. Most current piezoionic systems exhibit frequency responses similar to those of Merkel cells and Meissner corpuscles, with maximum potentials exceeding 15 mV, rendering them able to trigger an action potential. Thus, they could be used for neuromodulation, ionic skin or biointerfaces. Nonetheless, piezoionic systems with a frequency response similar to that of Pacinian corpuscles are still missing. The development of piezoionic systems capable of mimicking each type of mechanoreceptor is a step toward producing a more complex ionic skin that is able to fully mimic the intricate touch perception of the skin.

**Energy harvesting** appears as a promising application for piezoionics owing to their ability to convert mechanical energy into electrical energy.<sup>48</sup> Yet, piezoionic devices are less efficient than common energy harvesters with respect to their production of low output voltage in the few-hundred-millivolt range, with only a peak power per volume comparable to that of common harvesters.<sup>38,52,60</sup> While piezoelectric devices produce power densities in the range of 0.4–30  $\mu\text{W cm}^{-3}$ ,<sup>3,83</sup> piezoionics are reported with power densities in the range of 0.85–1.3  $\mu\text{W cm}^{-3}$ .<sup>38,52,60</sup> Despite these limitations, piezoionic

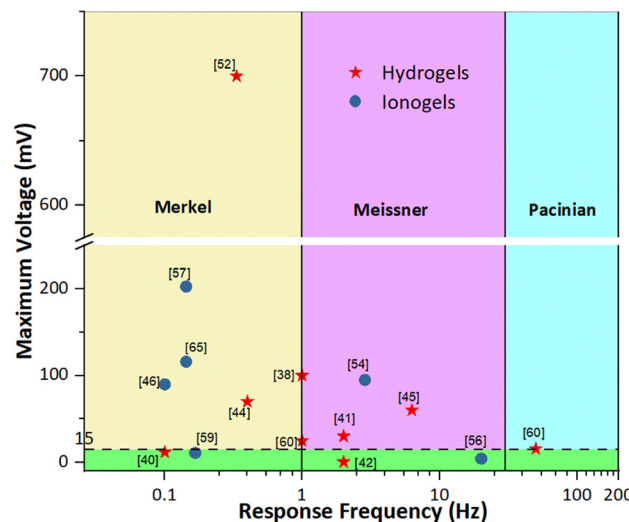


Fig. 11 Maximum voltage with respect to frequency response times of common polymeric ionic materials. Range of action potentials (green region), frequency range of Merkel cells (yellow region), frequency range of Meissner corpuscles (purple region) and frequency range of Pacinian corpuscles (teal region) are identified.

systems offer substantial potential for further improvement and are competitive with some low-performance piezoelectric harvesters. Nevertheless, mechanical-to-ionic transduction is relatively novel and has not been extensively studied, especially for energy harvesting, suggesting a promising avenue for enhancing the capabilities of piezoionic systems as next-generation energy harvesters.

Limitations for real-sensing devices persist as several challenges must still be overcome before piezoionic transducers can be translated into practical and reliable sensing technologies. These constraints, such as a slower response, impact the device performance, depending on the specific application. In this regard, overcoming these limitations is the cornerstone for achieving functional integration and ensuring long-term operational stability in real-world sensing environments. The strategies that have previously been developed for mitigating these limitations in the realm of soft sensor technologies afford promising avenues for the future adaptation of piezoionic devices, as described hereafter.<sup>84,85</sup> A primary limitation stems from the intrinsic water-dependent behaviour of piezoionic transducers, which can be mitigated through encapsulation strategies for minimizing water loss and enhancing environmental stability.<sup>38</sup> However, the encapsulation must be judiciously designed to preserve mechanical compliance, maintain ionic conductivity, and ensure long-term durability. This consideration is particularly critical for ionic-skin applications, where the mechanical properties of the device must closely match those of biological tissues. An alternative approach consists of developing water-retaining materials<sup>86,87</sup> that demonstrate remarkable stability under extreme temperature variations, thereby enabling reliable device performance through diverse environmental conditions. Aside from encapsulation and the development of water-retaining materials,



deep eutectic solvent-based systems have emerged as a promising alternative for ionic skins, offering superior properties than regular ionogels.<sup>88</sup> The implementation of all-solid-state systems represents another promising approach, offering liquid-free materials with moderate ionic conductivity, robust mechanical properties, and high thermal stability. As demonstrated by Ribeiro *et al.*,<sup>66</sup> who reported a PIL-based piezionic sensor, such materials exhibit exceptional compatibility for achieving stable piezionic performance. The absence of liquids (e.g., water) can mitigate dehydration and leakage, substantially extending a device's operational lifetime. Of particular relevance to ionic skin, tissue engineering and biointerface applications are stringent biocompatibility requirements, which can severely constrain the selection of suitable materials that can be safely interfaced with tissues.<sup>80,84</sup> While piezionic transducers possess tissue-like mechanical softness and ionic transport characteristics comparable to those of biological tissues, their stable operation under physiological conditions remains challenging due to dehydration, leaching, and compositional instability. Achieving robust adhesion and seamless integration with biological systems without perturbing native physiological functions also constitutes a major frontier for these applications.<sup>49,84</sup> Beyond hydration stability and biocompatibility, ensuring durability and long-term operational reliability certainly represent other crucial design objectives.<sup>84</sup> Soft electromechanical sensors are subjected to repeated mechanical and environmental stresses, underscoring the need for resilient, self-healing materials that support the realization of stable, long-lasting sensing platforms. For instance, the incorporation of reversible bonding interactions (similarly to supramolecular materials) can substantially enhance durability, improve mechanical performance, and extend the overall device lifespan.<sup>89</sup> For example, Hu *et al.*<sup>90</sup> developed a supramolecular ionic gel with self-healing capability for soft sensor applications based on a deep eutectic solvent, while Kim *et al.*<sup>54</sup> reported a piezionic sensor (PVDF swollen in EMIM-TFSI) integrating a similar autonomous self-healing functionality. Both the response and recovery times are key determinants of the performance of piezionic devices. They are influenced by mechanical hysteresis stemming from viscoelastic energy dissipation<sup>91</sup> and ionic hysteresis arising from the temporal mismatch between pressure-driven ion transport and diffusion-mediated re-equilibration.<sup>38,49</sup> Although piezionic transducers typically exhibit response and recovery times on the order of seconds and are suitable for soft wearable electronics, mechanical hysteresis continues to pose a significant challenge. In particular, low mechanical hysteresis is an imperative characteristic for soft sensors, facilitating the swift recovery of deformed materials, swift electrical signal response, and the maintenance of signal cyclic stability.<sup>92</sup> Among the strategies for reducing mechanical hysteresis, supramolecular architectures can distribute stress uniformly under repeated deformation, minimizing energy dissipation.<sup>91,93</sup> For example, Sun *et al.*<sup>93</sup> reported low-hysteresis supramolecular ionogels achieving *ca.* 11.7% hysteresis at 400% strain. Other strategies for reducing mechanical hysteresis include densely entangled

polymer networks, phase separation, or the incorporation of controlled microstructures, such as microcracks and microchannels, which guide deformation and facilitate recovery of the original shape.<sup>85,91</sup> To date, piezionic devices for energy harvesting and biointerfaces applications require rapid response and recovery times, making ionic hysteresis a critical challenge. Conductive pathways, as demonstrated by Dai *et al.*,<sup>49</sup> endow faster response and recovery times. For biointerfaces, particularly in neuromodulation, the stimulation frequencies of the device are crucial for achieving therapeutic efficacy (as determined by the response and recovery times).<sup>94</sup> For energy harvesters, slow mechanical-to-ionic transduction limits operational frequency, restricting energy conversion efficiency compared with conventional electromechanical sensors. Therefore, structural design strategies including gradient-like structures, controlled porosity, and microphase separation can enhance output voltages and efficiency. Careful attention to data acquisition, calibration, and signal processing is essential as piezionic transducers are sensitive to external noise, including capacitive and triboelectric interferences.<sup>38</sup> Ultimately, the convergence of these advances will enable the development of piezionic devices that are stable, reproducible, and fully compatible with the mechanical and operational demands of next-generation applications.

## Conclusions

Polymeric ionic materials undoubtedly represent the base for the next-generation of iono-electromechanical sensors with respect to their biomimetic mechanical-to-ionic transduction mechanism, their ability to mimic the production of biological signals and their transmission. Overall, a fluid pressure gradient is created under mechanical stimulation which drives fluid flow within the matrix. As a result, a transient separation between cations and anions takes place due to their different mobilities and interactions, breaking electrical neutrality and generating a transient voltage. Although the working principle of mechanical-to-ionic transduction in polymeric ionic materials is not yet fully understood, a foundational framework has been established that outlines the underlying transduction mechanism and the key parameters governing voltage generation.

We classified these parameters into two groups based on their principle of action: structural parameters primarily relate to the design of the polymer matrix, while operational parameters concern sensor assembly and practical operation. Among the structural parameters, the most critical ones are the type of polymer matrix, the nature and mobility of the ionic species, the conduction mechanism (single-ion *vs.* ion-pair), material dimensions (including thickness), charge density, crosslinking density, porosity, microphase separation, as well as the presence of gradient-like structures or conductive pathways. The performance of piezionic sensors is strongly governed by the type of polymer matrix and the mobility of the incorporated ionic species. While hydrogel- and iongel-based systems offer exceptionally high voltage outputs due to the



presence of liquid ion transporters, their long-term stability is limited by evaporation, leakage, or leaching. In contrast, solid-state polyelectrolyte systems eliminate these drawbacks, providing superior safety, durability, and suitability for skin- and health-monitoring applications. Importantly, single-ion conducting solid-state matrices, particularly those based on polyelectrolytes and poly(ionic liquid)s, are the most promising direction, as they enable stable ion-gradient formation, reduced voltage decay, and competitive output voltages (up to 190 mV). Ion mobility is governed by ion diffusion within the matrix, which is influenced by factors, such as ionic charge, size, concentration, and electrophoretic mobility. In single-ion conducting systems, optimal performance is achieved when the mobile ions are small, exhibit high charge delocalization, and show minimal coordination with the polymer matrix. By contrast, in ion-pair conducting systems, performance can be enhanced by selectively reducing the mobility of one ionic species, thereby facilitating the formation of stable charge gradients.

Thinner films are more favorable, as they enable higher voltage generation and faster response due to narrower force distribution and shorter poroelastic relaxation times. A high charge density is critical since a greater number of mobile ions per unit volume directly amplifies the generated output voltage. In contrast, the crosslinking density should be kept relatively low, because excessive crosslinking restricts fluid and ion transport, leading to a reduced voltage output and a slower response. A moderate degree may still be required to maintain mechanical robustness. Lower material density is preferable, as high density increases stiffness and reduces permeability, which slows fluid flow and extends recovery times. Overall, the most promising polymer matrices for piezionic sensors are therefore thin, lightweight, and moderately crosslinked systems with a high charge density. Such a combination maximizes ion transport efficiency, enhances voltage generation, and ensures fast response and recovery times under mechanical loading.

When speaking about additional structural design, the highest-performing piezionic polymer matrices based on their ion-pair mobility should combine small, well-distributed porosity and microphase-separated domains. An optimal porous structure is beneficial, as it reduces stiffness (enhancing electromechanical sensitivity) and increases charge separation efficiency. Smaller, well-distributed pores are especially effective, since they maximize ion mobility differences and improve voltage generation. The coexistence of hard and soft domains allows stress concentration in rigid phases, while enabling rapid ion transport in soft regions. For both single-ion and ion-paired systems, the creation of gradient-like architectures and the incorporation of directed conductive pathways and gating mechanisms are of great importance. By designing gradients for the ion type, charge density, stiffness, or geometry, the system can achieve controlled amplification, faster responses, and multifunctional sensing capabilities, such as discrimination between static and dynamic forces.

As mechanical-to-ionic transduction is relatively new and not yet extensively studied, there is currently no standardized

approach for assembling and testing piezionic sensors. Different authors employ diverse evaluation methods, making direct comparison of results challenging. While most studies report the generated voltage under varying mechanical loads, data on the relaxation time (how quickly the sensor can be reused without loss of sensitivity) and response time (how rapidly it responds to an applied load) are generally lacking. Despite these limitations, this review not only provides guidelines for designing efficient piezionic devices with an enhanced performance, but also outlines optimal strategies for sensor assembly and offers fundamental insights into the underlying piezionic mechanism. Ultimately, careful matrix design *via* the optimization of ionic mobility, crosslinking density, and electrode interfaces will be essential for advancing solid-state piezionic sensors as the leading platform for future applications.

## Author contributions

Conceptualization: J. A. G., C. P., J.-M. R., J. O.; investigation: J. A. G., V. S.; supervision: J.-M. R., J. O.; writing – original draft: J. A. G., J. O.; writing – review and editing: C. P., A. S., J.-M. R., J. O.; and funding acquisition: A. S., J.-M. R., J. O. All authors have read and agreed to the published version of the manuscript.

## Conflicts of interest

There are no conflicts to declare.

## Data availability

No primary research results, software or code have been included and no new data were generated or analysed as part of this review.

## Acknowledgements

We gratefully acknowledge support from the Belgian Federal Government Office of Science Policy (SSTC-PAI 6/27) as well as both Wallonia and the European Commission “FSE and FEDER”. The authors also acknowledge the PDR project “INFINITE” supported by the Fonds de la Recherche Scientifique (F.R.S.-FNRS) and the Luxembourg National Research Fund (FNR) (agreement number INTER/FNRS/21/16555380/INFINITE). J.-M.R. is an FNRS Research Director and a WEL-T Researcher. Some figures in this work were created with [BioRender.com](https://biorender.com).

## Notes and references

- 1 R. Cao, H. Tian, Y. Tian and X. Fu, *Adv. Sci.*, 2024, 11(11), 2302327.
- 2 S. Liu, S. Wang, L. Zou and W. Xiong, *Cell. Mol. Life Sci.*, 2021, 78, 5083–5094.

3 S. Maksimovic, M. Nakatani, Y. Baba, A. M. Nelson, K. L. Marshall, S. A. Wellnitz, P. Firozi, S.-H. Woo, S. Ranade, A. Patapoutian and E. A. Lumpkin, *Nature*, 2014, **509**, 617–621.

4 M. J. Caterina, *J. Clin. Invest.*, 2021, **131**, e1565871.

5 D. Julius, *Annu. Rev. Cell Dev. Biol.*, 2013, **29**, 355–384.

6 A. Yamada, J. Ling, A. I. Yamada, H. Furue and J. G. Gu, *Neuron*, 2024, **112**(8), 1286–1301.

7 L. Wang, L. Ma, J. Yang and J. Wu, *Cyborg Bionic Syst.*, 2021, 9843259.

8 A. Roe, R. Friedman and L. Chen, in *Handbook of Neurochemistry and Molecular Neurobiology: Sensory Neurochemistry*, ed. D. A. Johnson and A. Lajtha, Springer Science & Business Media, 2007, pp. 1–16.

9 K. Xiao, C. Wan, L. Jiang, X. Chen and M. Antonietti, *Adv. Mater.*, 2020, **32**(31), 2000218.

10 G. Sun, P. Wang, Y. Jiang, H. Sun, C. Meng and S. Guo, *Soft Sci.*, 2022, **2**, 17.

11 K. H. Ha, H. Huh, Z. Li and N. Lu, *ACS Nano*, 2022, **16**(3), 3442–3448.

12 J. Hu, G. Dun, X. Geng, J. Chen, X. Wu and T.-L. Ren, *Nanoscale Adv.*, 2023, **12**, 3131–3145.

13 Z. Zhang, *SHS Web Conf.*, 2023, **157**, 01026.

14 X. Zhang, J. Xu, Z. Chen, G. Zhu, A. Wei and D. Chen, *J. Alloys Compd.*, 2024, **1007**, 176408.

15 J. Chen, T. Song, X. Wang, Y. Zhou, T. Wang, X. Zhang and W. Han, *Nano Energy*, 2024, **131**, 110285.

16 L. Wang, H. Ning, S. Chen, Y. Huang, S. Chen, L. Wang and J. Peng, *Appl. Mater. Today*, 2024, **41**, 102474.

17 L. Liu, Y. Zhang, L. Tan, Y. Deng, X. Zheng, K. Tang and Y. Pei, *Chem. Eng. J.*, 2024, **499**, 155975.

18 Q. Li, Z. Zhang, L. Xu, X. Wang and Z. Li, *Sens. Actuators, A*, 2024, **378**, 115849.

19 J. Wang, Y. Zhong, S. Dai, H. Zhu, L. Wu, F. Gu and J. Ding, *ACS Appl. Nano Mater.*, 2022, **5**(9), 13227–13235.

20 M. Cheng, Y. Yuan, Q. Li, C. Chen, J. Chen, K. Tian and H. Deng, *J. Mater. Sci. Technol.*, 2025, **21**, 60–69.

21 V. Amoli, J. S. Kim, E. Jee, Y. S. Chung, S. Y. Kim, J. Koo and D. H. Kim, *Nat. Commun.*, 2019, **10**(1), 4019.

22 J. S. Kim, H. Choi, H. J. Hwang, D. Choi and D. H. Kim, *Macromol. Biosci.*, 2020, **20**(11), 2000147.

23 H. Huang, X. Ran, S. Wan, Y. Wang and H. Bi, *Nanoscale*, 2024, **16**(38), 17926–17933.

24 C. Liu, M. H. Uddin and K. Zhang, *Sens. Actuators, A*, 2024, **374**, 115519.

25 Y. Zhou, L. Zhao, Q. Jia, T. Wang, P. Sun, F. Liu and G. Lu, *ACS Appl. Mater. Interfaces*, 2022, **14**(49), 55109–55118.

26 N. Bai, L. Wang, Y. Xue, Y. Wang, X. Hou, G. Li and C. F. Guo, *ACS Nano*, 2022, **16**(3), 4338–4347.

27 P. Lu, L. Wang, P. Zhu, J. Huang, Y. Wang, N. Bai and C. F. Guo, *Sci. Bull.*, 2021, **66**(11), 1091–1100.

28 M. Zhong, L. Zhang, X. Liu, Y. Zhou, M. Zhang, Y. Wang and D. Wei, *Chem. Eng. J.*, 2021, **412**, 128649.

29 J. Luo, L. Zhang, T. Wu, H. Song and C. Tang, *Extreme Mech. Lett.*, 2021, **48**, 101279.

30 L. Zhen, M. Cui, X. Bai, J. Jiang, X. Ma, M. Wang and B. Yang, *Nano Energy*, 2024, **131**, 110188.

31 Y. Chen, C. Qin, Q. Sun and M. Wang, *Sens. Actuators, A*, 2024, **379**, 115970.

32 Y. Zhang, C. Liu, B. Jia, D. Ma, X. Tian, Y. Cui and Y. Deng, *npj Flexible Electron.*, 2024, **8**(1), 23.

33 X. Sui, Q. Mu, J. Li, B. Zhao, H. Gu, H. Yu and D. Hu, *Biosensors*, 2024, **14**(10), 508.

34 S. Zhao, C. Chen, Z. Wang, C. Pan and C. Yang, *InfoMat*, 2024, e12552.

35 J. Xu, H. Li, Y. Yin, X. Li, J. Cao, H. Feng and G. Zhu, *Flexible Electron.*, 2024, **6**(1), 62.

36 C. Wan, K. Xiao, A. Angelin, M. Antonietti and X. Chen, *Adv. Intell. Syst.*, 2019, **1**(7), 1900073.

37 S. Mirza, Y. Dobashi, E. Glitz, M. Farajollahi, S. Mirabbasi, S. Naficy and J. D. Madden, *Electroactive Polym. Actuators Devices (EAPAD)*, 2015, **9430**, 505–513.

38 Y. Dobashi, D. Yao, Y. Petel, T. N. Nguyen, M. S. Sarwar, Y. Thabet and J. D. Madden, *Science*, 2022, **376**(6592), 502–507.

39 J. Xu, Q. Li and D. Ho, *Mater. Horiz.*, 2024, **11**(22), 5709–5721.

40 Y. Dobashi, G. Allegretto, M. S. Sarwar, E. Cretu and J. D. Madden, *MRS Adv.*, 2016, **1**(1), 63–68.

41 J. Dai, Y. Xue, X. Chen, Z. Cao, L. Wang, J. Zhang and K. Xiao, *Device*, 2024, **2**(7), 100436.

42 B. Ma, K. Huang, G. Chen, Y. Tian, N. Jiang, C. Zhao and H. Liu, *Soft Sci.*, 2024, **4**, 8.

43 M. Burattini, R. Lippens, N. Baleine, M. Gerard, J. Van Meerssche, C. Geeroms and L. Thorrez, *Macromol. Biosci.*, 2023, **23**(7), 2300019.

44 J. Odent, N. Baleine, V. Biard, Y. Dobashi, C. Vancaeyzeele, G. T. Nguyen and J. M. Raquez, *Adv. Funct. Mater.*, 2023, **33**(3), 2210485.

45 F. Li, X. Cai, G. Liu, H. Xu and W. Chen, *Adv. Funct. Mater.*, 2023, **33**(32), 2300701.

46 W. Zhu, B. Wu, Z. Lei and P. Wu, *Adv. Mater.*, 2024, **36**(18), 2313127.

47 D. Ho, *ChemElectroChem*, 2024, **11**(3), e202300268.

48 K. Chen and D. Ho, *Aggregate*, 2024, **5**(1), e425.

49 P. G. De Gennes, K. Okumura, M. Shahinpoor and K. Kim, *J. Europhys. Lett.*, 2000, **50**(4), 513.

50 Z. Song, X. Cao and H. Huang, *Phys. Rev. E*, 2018, **97**(1), 012411.

51 Z. Song, X. Cao and H. Huang, *Phys. Rev. E*, 2018, **98**(3), 032404.

52 S. Wang, T. Yang, D. Zhang, Q. Hua and Y. Zhao, *Adv. Mater.*, 2024, **36**(36), 2405391.

53 M. Kilic, M. Bazant and A. Ajdari, *Phys. Rev. E: Stat. Phys., Plasmas, Fluids, Relat. Interdiscip. Top.*, 2007, **75**, 021503.

54 Y. R. Kim, G. Lim, H. Cho, J. Kim, J. Kim, J. Yeom and H. Ko, *Nano Energy*, 2024, **127**, 109749.

55 J. Zhao, S. Han, Y. Yang, R. Fu, Y. Ming, C. Lu and W. Chen, *ACS Nano*, 2017, **11**(9), 8590–8599.

56 Y. Liu, Y. Hu, J. Zhao, G. Wu, X. Tao and W. Chen, *Small*, 2016, **12**(36), 5074–5080.

57 C. Lu, X. Yu, Y. Chen, X. Chen and X. Zhang, *Chem. Eng. J.*, 2023, **463**, 142523.

58 J. I. Lee, H. Choi, S. H. Kong, S. Park, D. Park, J. S. Kim and M. S. Kang, *Adv. Mater.*, 2021, **33**(29), 2100321.



59 L. Li, J. Pan, L. Chang, Z. Liu, G. Wu and Y. Hu, *Chem. Eng. J.*, 2024, **482**, 148988.

60 X. Lu, Y. Chen, Y. Zhang, J. Cheng, K. Teng, Y. Chen and Q. An, *Adv. Mater.*, 2024, **36**(2), 2307875.

61 L. Li, Y. Shao, L. Jia, Z. H. Guo, Z. Li, Z. L. Wang and X. Pu, *Nano Energy*, 2025, **133**, 110477.

62 A. Adjaoud, G. T. Nguyen, L. Chikh, S. Péralta, L. Trouillet-Fonti, N. Uguen and C. Plesse, *Smart Mater. Struct.*, 2021, **30**(10), 105027.

63 Y. Ming, Y. Yang, R. P. Fu, C. Lu, L. Zhao, Y. M. Hu and W. Chen, *Adv. Mater. Technol.*, 2018, **3**(12), 1800257.

64 C. Lu, X. Chen and X. Zhang, *ACS Sens.*, 2023, **8**(4), 1624–1629.

65 C. Lu and X. Zhang, *Carbon*, 2024, **222**, 118956.

66 F. Braz Ribeiro, B. Ni, G. T. Nguyen, E. Cattan, A. S. Shaplov, F. Vidal and C. Plesse, *Adv. Mater. Interfaces*, 2023, **10**(10), 2202381.

67 A. S. Shaplov, R. Marcilla and D. Mecerreyres, *Electrochim. Acta*, 2015, **175**, 18–34.

68 C. Shan, Y. Wang, M. Liang, K. Lu, C. Xiong, W. Hu and B. Liu, *Energy Storage Mater.*, 2023, **63**, 102955.

69 Z. Zhu, L. Chang, T. Horiuchi, K. Takagi, A. Aabloo and K. Asaka, *J. Appl. Phys.*, 2016, **119**(12), 124901.

70 A. Gray-Weale, *Aust. J. Chem.*, 2009, **62**(4), 288–297.

71 Y. Hu and Z. Suo, *Acta Mech. Solida Sin.*, 2012, **25**(5), 441–458.

72 Q. M. Wang, A. C. Mohan, M. L. Oyen and X. H. Zhao, *Acta Mech. Sin.*, 2014, **30**, 20–27.

73 J. Grenier, H. Duval, F. Barou, P. Lv, B. David and D. Letourneur, *Acta Biomater.*, 2019, **94**, 195–203.

74 Y. Matsushita, *Encycl. Polym. Nanomater.*, 2014, 1–6.

75 H. Wang, Y. Xia, Z. Zhang and Z. Xie, *J. Mater. Chem. B*, 2023, **11**(37), 8883–8896.

76 G. Liu, Y. Deng, B. Ni, G. T. Nguyen, C. Vancaeyzeele, A. Brûlet and M. H. Li, *Small*, 2024, **20**(12), 2307565.

77 F. Hu, Y. Xue, J. Xu and B. Lu, *Front. Rob. AI*, 2019, **6**, 114.

78 H. C. Ates, P. Q. Nguyen, L. Gonzalez-Macia, E. Morales-Narváez, F. Güder, J. J. Collins and C. Dincer, *Nat. Rev. Mater.*, 2022, **7**(11), 887–907.

79 J. V. Vaghasiya, C. C. Mayorga-Martinez and M. Pumera, *npj Flexible Electron.*, 2023, **7**(1), 26.

80 H. J. Yoon, D. M. Lee, Y. J. Kim, S. Jeon, J. H. Jung, S. S. Kwak and S. W. Kim, *Adv. Funct. Mater.*, 2021, **31**(23), 2100649.

81 T. Denison and M. J. Morrell, *Neurology*, 2022, **98**(2), 65–72.

82 A. Gupta, N. Vardalakis and F. B. Wagner, *Commun. Biol.*, 2023, **6**(1), 14.

83 N. Sezer and M. Koç, *Nano Energy*, 2021, **80**, 105567.

84 Z. Lei, W. Xu and G. Zhang, *Smart Med.*, 2023, **2**(1), e20220026.

85 R. Papani, Y. Li and S. Wang, *Wiley Interdiscip. Rev.: Nanomed. Nanobiotechnol.*, 2024, **16**(3), e1961.

86 Z. Shen, J. Ma, Y. Cai, S. Li, D. Ruan, S. Dai and Z. Jia, *Cell Rep. Phys. Sci.*, 2023, **4**(12), 101741.

87 J. Wen, J. Tang, H. Ning, N. Hu, Y. Zhu, Y. Gong and T. Huang, *Adv. Funct. Mater.*, 2021, **31**(21), 2011176.

88 B. B. Hansen, S. Spittle, B. Chen, D. Poe, Y. Zhang, J. M. Klein and J. R. Sangoro, *Chem. Rev.*, 2020, **121**(3), 1232–1285.

89 M. Khatib, O. Zohar and H. Haick, *Adv. Mater.*, 2021, **33**(11), 2004190.

90 J. Hu, X. Yao, T. Li, X. Li, W. Wei and J. Liu, *ACS Appl. Polym. Mater.*, 2023, **5**(11), 9650–9658.

91 F. X. Liu, X. Jing, J. Yang, H. Y. Mi, F. Y. Feng and Y. J. Liu, *Nano Today*, 2025, **61**, 102601.

92 Z. Zhang, L. Qian, J. Cheng, C. Ma and G. Zhang, *Adv. Funct. Mater.*, 2024, **34**(37), 2402115.

93 B. Sun, K. Liu, B. Wu, S. Sun and P. Wu, *Adv. Mater.*, 2024, **36**(44), 2408826Low hysteresis.

94 I. Ezeokafor, A. Upadhyaya and S. Shetty, *Front. Neurosci.*, 2021, **15**, 671767.

